



HAL
open science

Herschel-ATLAS: multi-wavelength SEDs and physical properties of $250 \mu\text{m}$ selected galaxies at $z < 0.5$

D. J. B. Smith, L. Dunne, E. da Cunha, K. Rowlands, S. J. Maddox, H. L. Gomez, D. G. Bonfield, S. Charlot, S. P. Driver, C. C. Popescu, et al.

► **To cite this version:**

D. J. B. Smith, L. Dunne, E. da Cunha, K. Rowlands, S. J. Maddox, et al.. Herschel-ATLAS: multi-wavelength SEDs and physical properties of $250 \mu\text{m}$ selected galaxies at $z < 0.5$. *Monthly Notices of the Royal Astronomical Society*, 2012, 427, pp.703-727. 10.1111/j.1365-2966.2012.21930.x . hal-03645721

HAL Id: hal-03645721

<https://hal.science/hal-03645721>

Submitted on 6 Jun 2022

HAL is a multi-disciplinary open access archive for the deposit and dissemination of scientific research documents, whether they are published or not. The documents may come from teaching and research institutions in France or abroad, or from public or private research centers.

L'archive ouverte pluridisciplinaire **HAL**, est destinée au dépôt et à la diffusion de documents scientifiques de niveau recherche, publiés ou non, émanant des établissements d'enseignement et de recherche français ou étrangers, des laboratoires publics ou privés.

Herschel-ATLAS[★]: multi-wavelength SEDs and physical properties of 250 μm selected galaxies at $z < 0.5$

D. J. B. Smith,^{1,2†} L. Dunne,^{1,3} E. da Cunha,⁴ K. Rowlands,¹ S. J. Maddox,^{1,3} H. L. Gomez,⁵ D. G. Bonfield,² S. Charlot,⁶ S. P. Driver,^{7,8} C. C. Popescu,⁹ R. J. Tuffs,¹⁰ J. S. Dunlop,¹¹ M. J. Jarvis,^{2,27} N. Seymour,^{12,13} M. Symeonidis,¹³ M. Baes,¹⁴ N. Bourne,¹ D. L. Clements,¹⁵ A. Cooray,¹⁶ G. De Zotti,^{17,18} S. Dye,¹ S. Eales,⁴ D. Scott,¹⁹ A. Verma,²⁰ P. van der Werf,²¹ E. Andrae,¹⁰ R. Auld,⁵ S. Buttiglione,¹⁷ A. Cava,²² A. Dariush,^{5,23} J. Fritz,¹⁴ R. Hopwood,²³ E. Ibar,²⁴ R. J. Ivison,^{11,24} L. Kelvin,^{7,8} B. F. Madore,²⁵ M. Pohlen,⁵ E. E. Rigby,¹ A. Robotham,^{7,8} M. Seibert²⁵ and P. Temi²⁶

¹*School of Physics and Astronomy, University of Nottingham, University Park, Nottingham NG7 2RD*

²*Centre for Astrophysics, Science & Technology Research Institute, University of Hertfordshire, Hatfield, Herts AL10 9AB*

³*Department of Physics and Astronomy, University of Canterbury, Private Bag 4800, Christchurch 8140, New Zealand*

⁴*Max-Planck Institut für Astronomie, Königstuhl 17, 60115 Heidelberg, Germany*

⁵*School of Physics and Astronomy, Cardiff University, The Parade, Cardiff CF24 3AA*

⁶*Institut d'Astrophysique de Paris, CNRS, Université Pierre & Marie Curie, UMR 7095, 98bis bd Arago, 75014 Paris, France*

⁷*SUPA, School of Physics and Astronomy, University of St. Andrews, North Haugh, St. Andrews KY16 9SS*

⁸*International Centre for Radio Astronomy Research, University of Western Australia, 7 Fairway, Crawley, Perth, Western Australia WA6009, Australia*

⁹*Jeremiah Horrocks Institute, University of Central Lancashire, Preston PR1 2HE*

¹⁰*Max-Planck Institut für Kernphysik (MPIK), Saupfercheckweg, 69117 Heidelberg, Germany*

¹¹*Institute for Astronomy, University of Edinburgh, Royal Observatory, Blackford Hill, Edinburgh EH9 3HJ*

¹²*CSIRO Astronomy & Space Science, PO Box 76, Epping NSW 1710, Australia*

¹³*University College London, Department of Space & Climate Physics, Mullard Space Science Laboratory, Holmbury St. Mary, Dorking, Surrey RH5 6NT*

¹⁴*Sterrenkundig Observatorium, Universiteit Gent, Krijgslaan 281 Sg, B-9000 Gent, Belgium*

¹⁵*Astrophysics Group, Imperial College London, Blackett Laboratory, Prince Consort Road, London SW7 2AZ*

¹⁶*University of California, Irvine, Department of Physics & Astronomy, 4186 Frederick Reines Hall, Irvine, CA 92697-4575, USA*

¹⁷*INAF – Osservatorio Astronomico Di Padova, Vicolo Osservatorio 5, I-35122 Padova, Italy*

¹⁸*SISSA, Via Bonomea 265, I-34136 Trieste, Italy*

¹⁹*Department of Physics and Astronomy, 6224 Agricultural Road, University of British Columbia, Vancouver, BC V6T 1Z1, Canada*

²⁰*Astrophysics, Department of Physics, Denys Wilkinson Building, Keble Road, Oxford OX1 3RH*

²¹*Leiden Observatory, Leiden University, PO Box 9513, NL-2300 RA Leiden, the Netherlands*

²²*Departamento de Astrofísica, Facultad de CC. Físicas, Universidad Complutense de Madrid, E-28040 Madrid, Spain*

²³*Department of Physics, Imperial College, South Kensington Campus, London SW7 2AZ*

²⁴*UK Astronomy Technology Centre, Royal Observatory, Edinburgh EH9 3HJ*

²⁵*Observatories of the Carnegie Institution, 813 Santa Barbara St., Pasadena, CA 91101, USA*

²⁶*Astrophysics Branch, NASA Ames Research Center, Mail Stop 2456, Moffett Field, CA 94035, USA*

²⁷*Physics Department, University of the Western Cape, Private Bag X17, Bellville 7535, South Africa*

Accepted 2012 August 14. Received 2012 August 14; in original form 2011 September 26

ABSTRACT

We present a pan-chromatic analysis of an unprecedented sample of 1402 250 μm selected galaxies at $z < 0.5$ ($\bar{z} = 0.24$) from the *Herschel*-ATLAS survey. We complement our *Herschel* 100–500 μm data with UV–*K*-band photometry from the Galaxy And Mass Assembly (GAMA) survey and apply the MAGPHYS energy-balance technique to produce pan-chromatic spectral energy distributions (SEDs) for a representative sample of 250 μm selected galaxies

[★]*Herschel* is an ESA space observatory with science instruments provided by European-led Principal Investigator consortia and with important participation from NASA.

†E-mail: daniel.j.b.smith@gmail.com

spanning the most recent 5 Gyr of cosmic history. We derive estimates of physical parameters, including star formation rates, stellar masses, dust masses and infrared (IR) luminosities. The typical *H*-ATLAS galaxy at $z < 0.5$ has a far-infrared luminosity in the range 10^{10} – $10^{12} L_{\odot}$ (SFR: 1 – $50 M_{\odot} \text{ yr}^{-1}$) and thus is broadly representative of normal star-forming galaxies over this redshift range. We show that $250 \mu\text{m}$ selected galaxies contain a larger mass of dust at a given IR luminosity or star formation rate than previous samples selected at $60 \mu\text{m}$ from the *IRAS*. We derive typical SEDs for *H*-ATLAS galaxies, and show that the emergent SED shape is most sensitive to specific star formation rate. The optical–UV SEDs also become more reddened due to dust at higher redshifts. Our template SEDs are significantly cooler than existing IR templates. They may therefore be most appropriate for inferring total IR luminosities from moderate redshift sub-millimetre selected samples and for inclusion in models of the lower redshift sub-millimetre galaxy populations.

Key words: Galaxies: starburst.

1 INTRODUCTION

In the past couple of decades, our understanding of the Universe has flourished as a result of our new-found ability to observe in almost all regions of the electromagnetic spectrum. This advance is in no small part due to our ability to associate observations at different wavelengths with particular astrophysical phenomena and link them together, making modern astronomy truly pan-chromatic. By observing an astronomical source at multiple wavelengths, we may piece together its spectral energy distribution (SED) and by comparing the observed SED to models, we may infer the physical properties of the source (or sample of sources) that we are studying.

At ultraviolet (UV), optical and near-infrared (NIR) wavelengths, the SED of the average galaxy is dominated by emission from stars; there are many tens of different models to which we may compare our observations, in the hope of understanding the stellar components of astrophysical sources (e.g. Jimenez et al. 1995, 2004; Fioc & Rocca-Volmerange 1997; Anders & Fritze-v. Alvensleben 2003; Bruzual & Charlot 2003; Pietrinferni et al. 2004; Maraston 2005; Vázquez & Leitherer 2005). Such SED model analysis may be used to determine the basic properties of a galaxy’s stellar components, such as its age, metallicity or stellar mass (see e.g. Smith & Jarvis 2007; Carter et al. 2009; Collins et al. 2009; Pacifici et al. 2012; Pforr, Maraston & Tonini 2012).

While the UV to NIR emission tells us about the stellar content of a normal galaxy (subject to correcting for attenuation by dust of the different stellar components; Charlot & Fall 2000; Pierini et al. 2004; Tuffs et al. 2004), the far-infrared (FIR) and sub-millimetre wavelengths probe its cool dust content, which is itself crucial to our understanding of star formation, since approximately half of the energy ever radiated by stars has been absorbed by dust and re-radiated at these wavelengths (e.g. Puget et al. 1996; Fixsen et al. 1998). The sub-millimetre region has been a difficult part of the electromagnetic spectrum in which to conduct large galaxy surveys (e.g. Smail, Ivison & Blain 1997; Hughes et al. 1998; Eales et al. 1999). Previous ground-based sub-millimetre surveys had to be either pointed at pre-selected targets or limited to relatively small regions of sky covering areas of $< 1 \text{ deg}^2$ (Coppin et al. 2006; Weiß et al. 2009). The combined effects of the large negative k -correction at these wavelengths, sensitivity and the steep number counts have meant that the average $850 \mu\text{m}$ selected sub-millimetre galaxy is extremely luminous (10^{12} – $10^{13} L_{\odot}$) and resides at high redshift ($z \sim 2$, e.g. Chapman et al. 2005). Few relatively local galaxies

have been found in blind sub-mm surveys, due to the small local volumes probed in these surveys coupled with the observing wavelength targeting the faint Rayleigh–Jeans tail of the dust SED at low redshift. Our understanding of the local Universe at sub-mm wavelengths has so far come from targeted surveys such as the SCUBA Local Universe Galaxy Survey (SLUGS; Dunne et al. 2000), which observed a sample of 184 *IRAS*- and optically selected galaxies (Vlahakis, Dunne & Eales 2005). Pre-selected galaxies in this way can lead to biases if there are classes of sub-mm emitting galaxies which are not bright at either optical or at $60 \mu\text{m}$ wavelengths. The SLUGS was also limited to very nearby galaxies and so could not address the question of evolution of sub-mm properties in the relatively recent past.

With the advent of the PACS (Poglitsch et al. 2010) and SPIRE (Griffin et al. 2010) instruments aboard the ESA *Herschel Space Observatory* (Pilbratt et al. 2010), we now have our first opportunity to survey a large area of sky at sub-mm wavelengths. The angular resolution and sensitivity of *Herschel* allow us to robustly determine the counterparts to thousands of local sub-millimetre *selected* galaxies across the whole electromagnetic spectrum, thus gaining invaluable insight into their physical processes. This paper uses a sample from the *Herschel* Astrophysical TeraHertz Large Area Survey (*H*-ATLAS; Eales et al. 2010) and presents fits to their UV–sub-mm SEDs. This is the first relatively local ($z < 0.5$) sub-mm selected sample for which such complete SED modelling has been performed. This work is based on only 3 per cent of the final data set, but is still large enough to provide a statistical study of the optical and IR properties of > 1000 $250 \mu\text{m}$ selected galaxies, and templates for SEDs which can be applied more widely.

Studies of the multi-wavelength properties of the relatively small number of galaxies detected in sub-millimetre surveys have been extensive (e.g. Swinbank et al. 2009). At high redshifts, galaxy star formation rates have been frequently estimated based on a single sub-millimetre flux measurement (e.g. at $850 \mu\text{m}$), and a local template SED belonging to e.g. M82 or Arp 220 (e.g. Silva et al. 1998), chosen not because they are known to be representative of the average sub-millimetre galaxy, but rather because they are comparatively well studied.

Another commonly used method of describing FIR galaxy SEDs is to assume one or more components with modified blackbody (the so-called ‘grey-body’) profiles. In these simple parametrizations, the observed flux densities depend only on the temperature (T) and dust emissivity index (β), which may be either assumed or derived,

Table 1. The coverage of the 250 μm sources in our catalogue, detailing which sources are detected in which FIR bands, and detailing the number of sources with photometry from *GALEX*. The sensitivity limits indicate the properties of the input catalogues; note that in order for a source to have aperture photometry, we require a 5σ 250 μm detection with an $R \geq 0.8$ counterpart from the upper row.

Instrument: Band: Catalogue sensitivity:	<i>Herschel</i> -SPIRE			<i>Herschel</i> -PACS			<i>IRAS</i>	<i>GALEX</i>		
	250 μm	350 μm	500 μm	160 μm	100 μm	Both	60 μm	FUV	NUV	Both
	$\geq 5\sigma$	> 0	> 0	$\geq 5\sigma$	$\geq 5\sigma$	$\geq 5\sigma(\times 2)$	$\geq 5\sigma$	$\geq 5\sigma$	$\geq 5\sigma$	$\geq 5\sigma(\times 2)$
N (detections)	6621	5346	1717	304	151	117	34			
N (Galaxies, $R > 0.8$)	2417	1636	344	245	142	111	34			
Aperture photometry	1402	902	170	197	116	93	24	529	726	522
z_{spec}	1095	710	139	199	118	98	33			
Aperture photometry and z_{spec}	1052	682	128	186	108	89	24	520	700	513

depending on the available observations. Such simple grey-body profiles have been widely shown to broadly reproduce the sparsely sampled FIR SEDs of galaxies at all redshifts (e.g. Dunne et al. 2000; Blain et al. 2002; Blain, Barnard & Chapman 2003; Kóvács et al. 2006; Pope et al. 2006; Dye et al. 2010), although when the SED is sampled from 60 μm to the sub-mm additional grey-body components may be required to reproduce the observations (e.g. Dunne & Eales 2001; Smith et al. 2010; Galametz et al. 2011; Dale et al. 2012).

Empirical templates have been created for use with sparsely sampled FIR data based on observations of small samples of local galaxies with good coverage from mid- to far-infrared wavelengths (e.g. Chary & Elbaz 2001; Dale & Helou 2002; Rieke et al. 2009). Selecting galaxies at shorter FIR wavelengths tends to favour those with substantial warm dust components, which may not be representative of populations selected at longer wavelengths with *Herschel* and ground-based sub-mm instruments. Several studies have found that sub-mm selected galaxies (so far mostly at higher redshifts) may have colder dust than their local equivalents at similar FIR luminosities (e.g. Coppin et al. 2006; Pope et al. 2006; Hwang et al. 2010; Magnelli et al. 2012).

In this paper, we use a model that relies on energy balance – the idea that the energy absorbed by dust at UV and optical wavelengths must be re-radiated in the FIR – combined with a statistical fitting approach, to consistently model each galaxy’s full SED, and gain robust constraints on the star formation activity, stellar and dust content of 250 μm selected galaxies from *H-ATLAS*.

In Section 2, we discuss the *Herschel*-ATLAS survey and the multi-wavelength data used in generating the catalogue, while in Section 3 we discuss the SED-fitting method used in the analyses which we present in Section 4. In Section 5, we compare our median SEDs with other templates available, and in Section 6 we present some conclusions based on our results for the population of sub-millimetre galaxies in general. Throughout this paper, we use a standard cosmology with $H_0 = 71 \text{ km s}^{-1} \text{ Mpc}^{-1}$, $\Omega_M = 0.27$ and $\Omega_\Lambda = 0.73$, and an initial mass function (IMF) from Chabrier (2003).

2 CATALOGUE CONSTRUCTION

The *Herschel*-ATLAS (Eales et al. 2010) is the widest area survey being conducted with *Herschel* covering 570 deg^2 of sky in five FIR–sub-mm bands from 100–500 μm . One primary aim of *H-ATLAS* is to provide a census of dust and obscured star formation in the local Universe, with galaxies selected on the basis of their dust mass for the first time. Our current study is based on the *Herschel*-ATLAS Science Demonstration Phase data (SDP)

covering $\sim 14 \text{ deg}^2$ centred on the 9 h Galaxy And Mass Assembly (GAMA) field (Driver et al. 2011). The SPIRE and PACS map-making procedures are described in Pascale et al. (2011) and Ibar et al. (2010). From these maps, a catalogue of sources which are $\geq 5\sigma$ in any of the three SPIRE bands was produced using the MADX algorithm (Maddox et al., in preparation) and described in detail in Rigby et al. (2011). PACS sources were added to the catalogue based on the flux in apertures placed at the locations of SPIRE 250 μm sources. The catalogue we used for this sample is 250 μm selected and contains 6621 sources at $> 5\sigma$ (though not all of these are detected in all other bands – see below and Table 1). The 5σ point source flux limits are 132, 126, 32, 36 and 45 mJy in the 100, 160, 250, 350 and 500 μm bands, respectively (and including confusion), with beam sizes of approximately 9, 13, 18, 25 and 35 arcsec full width at half-maximum (FWHM) in the same five bands.

A likelihood-ratio analysis (LR; Sutherland & Saunders 1992; Ciliegi et al. 2005) was performed to identify robust optical counterparts to the sub-millimetre selected sources, using the SPIRE 250 μm channel and Sloan Digital Sky Survey (SDSS) r -band positions down to a limiting magnitude of SDSS r modelmag = 22.4. The method used is described in detail in Smith et al. (2011), but to summarize, the LR method uses both positional and photometric information of both individual sources and the population in general to quantify the reliability, R (or equivalently, the probability), of an association between two sources. Star–galaxy separation was performed following a method similar to that in Baldry et al. (2010), and the LR calculations were applied to each population separately, as the 250 μm properties of stars and galaxies are quite different (see Smith et al. 2011). For this study, we have chosen a reliability limit of $R \geq 0.8$ which gives 2417 250 μm sources with reliable galaxy counterparts, and a contamination rate of less than 5 per cent. We have also removed the five gravitationally lensed SMGs identified in Negrello et al. (2010) from the subsequent analysis.

These data were combined with the GAMA (Driver et al. 2011) catalogue over the same field (Hill et al. 2011), which contains thousands of spectroscopic redshifts, in addition to r -band-defined aperture-matched photometry for 1402 of the reliable galaxy counterparts. Since we require well-sampled multi-wavelength SEDs to constrain the physical properties of these 250 μm selected galaxies, we base our analysis on this sub-sample of 1402 galaxies, with optical/NIR aperture-matched photometry. The r -defined aperture-matched photometry is based on pixel- and seeing-matched images derived from the SDSS (York et al. 2000) and the UK Infrared Deep Sky Survey (UKIDSS) Large Area Survey (LAS; see e.g. Lawrence et al. 2007) in the *ugrizYJHK* bands. Additional photometry in the Galaxy Evolution Explorer (*GALEX*) far- and near-UV channels has been included from the *GALEX*-GAMA survey (Seibert et al., in preparation), as have spectroscopic redshifts from

the GAMA, SDSS and 6dFGS surveys. There are 1052 sources with spectroscopic redshifts and r -defined aperture photometry. For the 350 sources with no spectroscopic redshifts available, we adopt ANN z -derived (Collister & Lahav 2004) neural network photometric redshifts from Smith et al. (2011).

All available photometry has been brought on to the AB magnitude system. Simulations have shown that the photometric errors estimated by `SEXTRACTOR` (Bertin & Arnouts 1996) are underestimated by a factor of 4 in the GAMA resampled images (Hill et al. 2011); this factor was applied to the catalogue values. A further 0.1 magnitude error was added in quadrature to all optical and NIR photometry to account for the global uncertainties in the total flux measurements and calibrations between the various surveys.

Additional photometry was compiled for known detections from the *InfraRed Astronomical Satellite* (*IRAS*) Faint Source Catalogue (Moshir, Kopman & Conrow 1992; Wang & Rowan-Robinson 2009), using a 2 arcsec maximum match radius between cross-identified counterpart positions, including those sources with updated optical counterparts based on the higher-quality SPIRE and PACS images discussed in Smith et al. (2011). As noted in Table 1, there are 34 sources with detections in the *IRAS* 60 μm band. The errors on the *IRAS* fluxes were assumed to be 20 per cent (including calibration error) and we included upper limits in the *IRAS* 12, 25 and 60 μm channels based on the 5σ sensitivity limits given in Wang & Rowan-Robinson (2009).

To reflect the uncertainty in the SPIRE and PACS photometric calibration, the SPIRE errors had a factor of 15 per cent added in quadrature to the catalogue values, and the PACS errors had 10 and 20 per cent added in quadrature to the errors in the 100 and 160 μm bands, respectively (e.g. Griffin et al. 2010; Poglitsch et al. 2010). Although we only require 250 μm fluxes for the FIR selection, we include SPIRE fluxes in our input catalogue for each SPIRE band, irrespective of the signal-to-noise ratio in the 350 and 500 μm bands, provided that their measured flux is positive. For PACS, we only include those sources detected at $\geq 5\sigma$ significance in each band. This is due to residual $1/f$ noise in the current version of the PACS maps which limits the level at which we can extract reliable photometry at this current time. We plan to alleviate these problems in future releases.

The number of sources with coverage in each of the FIR photometric bands, as well as the number of sources with aperture-matched photometry and spectroscopic redshifts, are listed in Table 1. To summarize, our analysis will focus on a sub-sample of 1402 (i.e. 21 per cent) of the 5σ 250 μm detections for which well-matched multi-wavelength data are available.

2.1 The impact of selection effects

Since the sample presented in this paper is not selected purely at 250 μm , and relies on the identification of an optical counterpart brighter than 22.4 mag in the SDSS r -band data, it is necessary to consider the impact that this additional selection criterion might have on the results of this study.

In the top panel of Fig. 1, we show the variation in r -band magnitude for a representative template SED based on the galaxies in our sample (see Section 4.3 for more details of how this SED template was derived). At each redshift being considered, we fix the 250 μm flux of the template to the 5σ limit of our survey data (which corresponds to ~ 12.5 mag in the AB system), and convolve the template with the SDSS r -band filter curve to determine the expected r -band magnitude that would be observed. We are then able to compare these values to the limits for the cross-identification

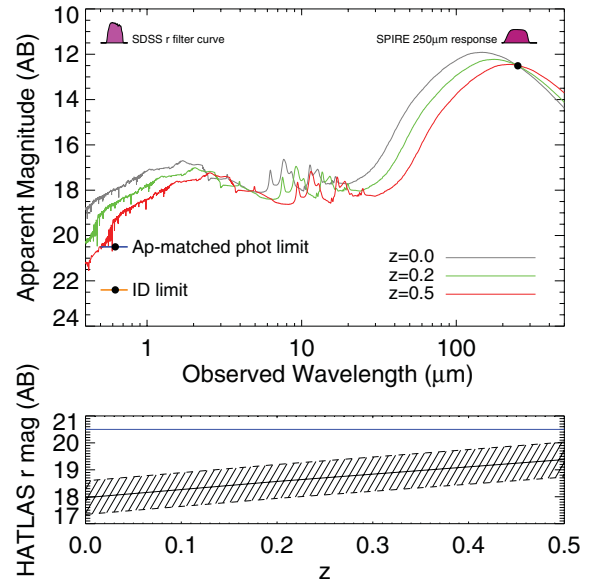


Figure 1. Top: expected magnitude of a median 250 μm selected galaxy template (discussed in Section 4.3) normalized to the H -ATLAS 250 μm flux limit at redshifts between $0.0 < z < 0.5$. The r -band limits for the optical cross-identification from Smith et al. (2011) and the GAMA aperture-matched photometry (Hill et al. 2011) are shown by the labelled blue and orange lines on the left-hand side. The response curves of SPIRE at 250 μm and the SDSS r -band data are shown in the top corners. Bottom: the variation of the expected brightness of a median 250 μm selected galaxy template in the SDSS r band as a function of redshift. The aperture-matched photometry limit of $r_{\text{petro}} = 20.5$ is shown by the blue horizontal line (i.e. the same colour as in the upper panel); the median 250 μm selected galaxy is at least a magnitude brighter than the r -band aperture-matched photometry limit even out to $z \sim 0.5$. The shaded area corresponds to the range of SEDs in the H -ATLAS template SED.

($r_{\text{model}} = 22.4$ mag) and for the GAMA aperture-matched photometry ($r_{\text{petro}} = 20.5$ mag), both of which are shown as the black labelled points and coloured lines in the upper panel. In the bottom panel of Fig. 1, we compare the predicted observed r -band magnitude as a function of redshift (solid line, with the surrounding shaded region corresponding to the uncertainty in the H -ATLAS template SED). The GAMA aperture-matched photometry limit is shown as a horizontal blue line. This shows that typical 250 μm selected galaxies should still be more than a magnitude brighter than the aperture-matched photometry limit even out to $z = 0.5$.

We may still lose galaxies of certain types from the sample at higher redshifts due to the optical limit, such as those with higher dust obscurations (i.e. higher 250 μm to r -band flux ratios). To investigate this further, in Fig. 2 we show histograms of the ($r - 250 \mu\text{m}$) colour (in AB magnitudes) of those galaxies with reliable counterparts in our sample, for different redshifts spanning $0.0 < z < 0.4$. Counterparts with aperture-matched photometry in the GAMA catalogue (i.e. those galaxies to which we apply our SED fitting method) are shown as the filled grey histograms, while galaxies without are hatched red. The orange vertical dashed line indicates the ($r - 250 \mu\text{m}$) colour of sources at the sensitivity limits in both the r band and 250 μm data, while the blue vertical dotted line shows the same colour for sources at the 250 μm flux limit and the nominal completeness limit for the GAMA photometry (20.5 mag in Petrosian magnitudes). It is clear from Fig. 2 that our r -band selection criterion does not prevent us from obtaining a representative sample of 250 μm sources with a full spread of ($r - 250 \mu\text{m}$)

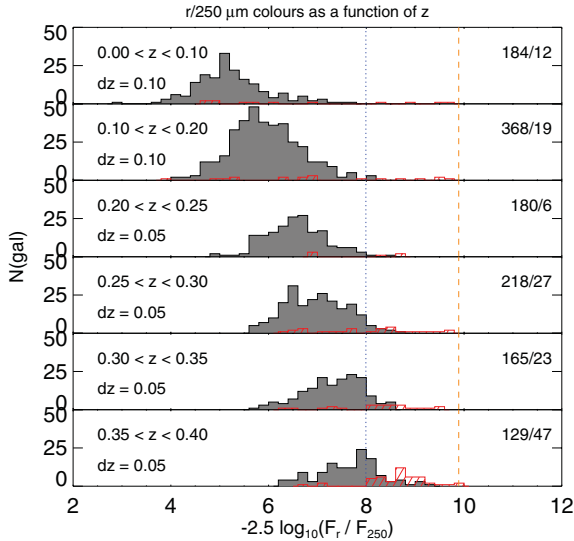


Figure 2. The $(r - 250 \mu\text{m})$ colours (in AB magnitudes) of the galaxies in our sample for different bins of redshift from $0.0 < z < 0.10$ (top) to $0.35 < z < 0.40$ (bottom). The grey histograms represent those galaxies for which we have aperture-matched photometry from the $u-K$ bands from the GAMA survey, while the dashed red histograms show the colours of those galaxies for which this aperture-matched photometry is not available (these are fainter than $r_{\text{petro}} = 20.5$ or below $\delta = -1^\circ$ declination due to the GAMA magnitude limit, and to the peculiarities of the GAMA/H-ATLAS survey overlap, respectively). The number of sources falling into each of these categories is shown in the top-right-hand corner of each panel. The vertical dashed line indicates the $(r - 250 \mu\text{m})$ colour corresponding to the sensitivity limits of our r -band and $250 \mu\text{m}$ catalogues, while the vertical dotted line indicates the colour defined by the magnitude limit for the GAMA aperture-matched photometry relative to the $250 \mu\text{m}$ flux limit. It is clear that we sample a representative range of $250 \mu\text{m}$ selected galaxy colours out to $z \approx 0.35$, but beyond this we are only sensitive to the less obscured part of the population.

colours, at least out to $z < 0.35$. At redshifts higher than $z \sim 0.35$, however, the r -band selection criterion does suggest that we are biased towards the lower obscuration sources (see also Dunne et al. 2011).

3 METHOD

3.1 SED modelling

We use the model of da Cunha, Charlot & Elbaz (2008; hereafter DCE08¹) to interpret the panchromatic SEDs of the galaxies in our *Herschel-ATLAS/IRAS/GAMA/GALEX* data set in terms of physical properties related to their star formation activity and dust content. This physically motivated model relies on an energy balance technique to interpret the (attenuated) stellar emission at UV, optical and NIR wavelengths consistently with the dust emission at mid-/far-infrared and sub-millimetre wavelengths. Therefore, this model is ideal to interpret the multi-wavelength observations available for this sample of galaxies. Here we briefly summarize the main features of this model; for more details, we refer to the exhaustive description provided in DCE08.

The dust-free UV to NIR emission from stellar populations in galaxies is computed using the latest version of the Bruzual &

Charlot (2003) stellar population synthesis models (Bruzual 2007; Charlot & Bruzual, in preparation). The attenuation of starlight by dust is described by the two-component prescription of Charlot & Fall (2000), which also provides the total energy absorbed by dust in the birth clouds (i.e. molecular clouds where stars form) and in the ambient (i.e. diffuse) interstellar medium (ISM). The spectral distribution of the energy re-radiated by dust at infrared and sub-millimetre wavelengths is then computed by assuming that the energy re-radiated by dust in the birth clouds and diffuse ISM is equal to the energy absorbed, and that starlight is the only significant source of heating [i.e. that there is no active galactic nucleus (AGN) contribution]. In stellar birth clouds, the dust emission is described as a sum of three components: polycyclic aromatic hydrocarbons (PAHs), hot mid-infrared continuum and warm dust in thermal equilibrium with temperature in the range 30–60 K. In the ambient ISM, the emission by dust is described using these three components (whose relative proportions are fixed for simplicity), plus a component of cold dust in thermal equilibrium with temperature in the range 15–25 K. The prior distribution of both the warm and cold dust temperatures is flat, such that all temperatures between the bounds of the prior have the same probability.² The hot and cold dust components of the spectrum are assumed to be optically thin, and are described in the same way as in DCE08 using modified greybody template spectra, $\propto \kappa_\lambda B_\lambda(T)$, with an emissivity index $\beta = 1.5$ and 2.0 for the warm and cold components, respectively, and dust mass absorption coefficient approximated as a power law, such that

$$\kappa_\lambda \propto \lambda^{-\beta} \quad (1)$$

with the normalization defined such that $\kappa_{850 \mu\text{m}} = 0.077 \text{ kg}^{-1} \text{ m}^2$ as in Dunne et al. (2000).

The simplicity and versatility of the DCE08 model make it ideal to interpret our rich multi-wavelength data set, as it allows us to derive statistical constraints (including probability density functions, hereafter PDFs) for several physical properties of the galaxies (such as star formation rate, stellar mass, dust attenuation, dust luminosity measured between 3 and $1000 \mu\text{m}$, dust temperature and dust mass), from the consistent modelling of their observed UV to sub-millimetre SEDs. To do so, we adopt the Bayesian approach used in DCE08 (see also da Cunha et al. 2010, hereafter dC10).

We use two stochastic libraries of models, as described in DCE08; the first contains 25 000 stellar population models, including a wide range of star formation histories, metallicities and dust attenuations, while the second consists of 50 000 dust emission models including a large range of dust temperatures and fractional contributions of PAHs, hot mid-infrared continuum, warm dust and cold dust to the total infrared luminosity. These two libraries are combined by associating models with similar values of $f_\mu = L_{\text{dust}}^{\text{ISM}} / L_{\text{dust}}^{\text{tot}}$ (the fraction of total dust luminosity contributed by the diffuse ISM), which are scaled to the same total dust luminosity $L_{\text{dust}}^{\text{tot}}$. For each combined model spectrum, we compute a library of synthetic photometry making use of the filter transmission curves for the same photometric bands as our observations, at intervals of $dz = 0.01$. We do not consider redshift to be a free parameter in our SED fits, and use either the spectroscopic redshift or the best-fitting photometric redshift from Smith et al. (2011) for these purposes. For ease of reference, some of the output parameters to which we refer in this analysis are summarized in Table 2.

¹ The DCE08 models are publicly available as a user friendly model package MAGPHYS at <http://www.iap.fr/magphys>.

² Our choice of prior distribution for the cold dust temperature is discussed in more detail in Appendix A.

Table 2. Summary of the SED model parameters used in this paper. For a more detailed description of each parameter, see DCE08.

Parameter	Definition
f_{μ}	Fraction of total dust luminosity contributed by the diffuse ISM
sSFR	Specific star formation rate is defined as the star formation rate per unit stellar mass, averaged over the last 0.1 Gyr, units of yr^{-1}
SFR	Star formation rate averaged over the last 0.1 Gyr in $M_{\odot} \text{yr}^{-1}$
M_{dust}	Dust mass in solar units, M_{\odot}
L_{dust}	Dust luminosity integrated between 3 and 1000 μm , in units of L_{\odot}
M_{stars}	Galaxy stellar mass in units of M_{\odot}
T_{cold}	Temperature of the cold dust in thermal equilibrium in the diffuse ISM

3.2 Spectral fits

We use the `MAGPHYS` model to fit the observed SEDs for the 1402 *Herschel*-ATLAS sources with robust (i.e. reliability >0.8) counterparts and matched-aperture photometry in the GAMA catalogue. For each galaxy, we compared the observed UV to sub-mm fluxes to the predicted fluxes of every pair of models in the stochastic libraries satisfying the energy balance criterion, by computing the χ^2 goodness-of-fit parameter for each model. This allowed us to build the PDF of any given physical parameter for the observed galaxy by weighting the value of that parameter in each model by the probability $\exp(-\chi^2/2)$. We then determine the median value of each PDF, corresponding to our best estimate for each parameter. We also determine an associated uncertainty, which corresponds to the 16th and 84th percentiles of the PDF. We note that the PDFs generated in this analysis are marginalized; this is particularly important since by definition they include parameter uncertainties due to e.g. the co-variances between parameters in the model. In what follows, the values of the physical properties of the galaxies mentioned refer to the median values of the PDF unless explicitly stated otherwise. We also create ‘stacked PDFs’ when discussing the parameter properties of samples of sources; this procedure is described fully in Appendix A1 but is designed to give our best estimate of the distribution of parameter values for sources in a sample convolved with our ability to constrain them. In addition to the PDFs for each model parameter, we also obtained the best-fitting model SED for each galaxy, which is the model that minimizes χ^2 .

It is important to determine whether or not the best-fitting model reasonably reproduces our observed data, which are not uniform across the sample. Since neighbouring photometric bands are not independent of one another, we conducted several sets of simulations, designed to empirically estimate the variation of the number of degrees of freedom in our spectral fits, as a function of the number of bands of input photometry available for a particular galaxy. The details of these simulations are presented in detail in Appendix B. To summarize, we determined a 99 per cent confidence interval on χ^2 , which depends solely on the number of photometric detections for a particular source, such that if the derived value of χ^2 is higher than the upper bound of the interval, there is only a <1 per cent chance that the galaxy is well described by our model, and is then removed from our sample.

We find that ~ 92 per cent of our sample are well described by our model. The galaxies with larger χ^2 values than our limit may have problems with photometry, contributions from AGN components, be lensed systems, have catastrophic photometric redshift errors, etc. Inspection of the bad fits (~ 8 per cent) reveals that the vast majority are due to serious problems with the aperture-matched photometry (e.g. catastrophic failures in multiple bands), while at least one is a QSO, and there are two possible lensed objects with far-IR colours not consistent with the redshifts of their $R \geq 0.80$ counterparts, similar to those discussed in Negrello et al. (2010).

We note that there are 320 galaxies in our sample which rely on photometric redshift estimates, of which 126 lie at $z < 0.35$, where our sample is thought to be representative of the broader 250 μm selected population. Nine per cent of those galaxies relying on photometric redshifts have χ^2 values outside the range of acceptable values, as compared with seven per cent of those galaxies with spectroscopic redshifts, suggesting that sources with catastrophic photometric redshift errors do not make up the majority of unreliable SED fits.

Finally, we note that dC10 conducted a series of tests of this SED-fitting model using a local galaxy sample detected with SDSS and *IRAS*, and demonstrated the general robustness of the technique to the effects of inclination. They showed that while weak inclination effects may be present (using the ratio of the apparent major and minor axes of each particular galaxy as a proxy for inclination), they do not dominate the dispersion in estimates of galaxy properties.

4 RESULTS

Here we present the results of our SED-fitting analysis. For each galaxy, we not only determine best-fitting SEDs (Fig. 3), but also the PDFs for each parameter (Fig. 4). The parameters that we focus on are those shown in Fig. 4 (namely M_{dust} , L_{dust} , M_{stars} , f_{μ} , SFR, sSFR, $M_{\text{dust}}/M_{\text{stars}}$ and $M_{\text{dust}}/L_{\text{dust}}$), since we are interested in investigating the star formation activity and dust mass of normal, star-forming galaxies. Our sample represents almost an order of magnitude’s improvement upon the largest sub-mm selected samples until now, even though the *H*-ATLAS SDP data comprise only ~ 3 per cent of the total eventual *H*-ATLAS data set.

4.1 Importance of the available infrared observations

Given the inhomogeneous set of data which we have compiled for the *H*-ATLAS sample, it is important to have some understanding of the sensitivity of the derived physical parameters to the absence/presence of data at certain wavelengths. Some tests of this nature were performed by DCE08 and dC10, and demonstrated that the results derived were generally robust, although certain parameters (e.g. sSFR) are better constrained when UV data are included, for example. Our concerns for this study relate to determining the reliability of the estimates of dust luminosity, SFR and mass trends. Given that not all galaxies in the sample have data spanning the peak of their rest-frame FIR SED (from *IRAS* or PACS), we need to assess the impact of this heterogeneity on our results. We have performed three tests. The first test was to determine the reliability of our method when only *IRAS* data between 60 and 100 μm are used to constrain the FIR SED; secondly, we attempted to determine the influence of incomplete PACS data on our results, and finally, we attempted to probe the reliability of our results in the absence of

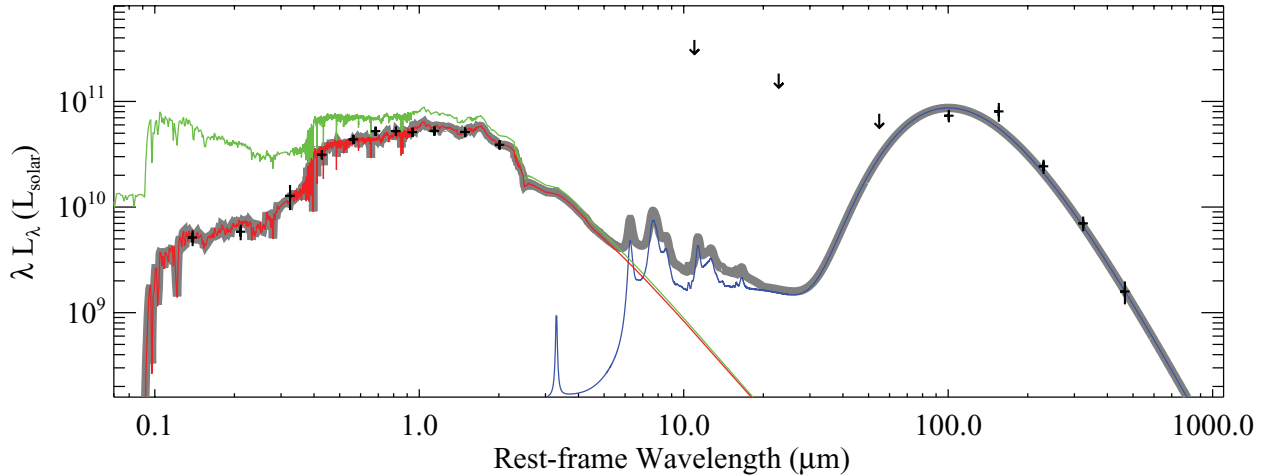


Figure 3. An example of best-fitting SED for one of the galaxies in our sample (H-ATLAS J090713.1-000322). This SED is derived based on our compiled data from SPIRE and PACS, plus upper limits at 12, 25 and 60 μm from *IRAS*, and aperture-matched photometry from u - K bands as well as photometry in the *GALEX* FUV and NUV bands. The data points are shown as the black crosses, with the error bars as discussed in Section 2. The upper limits are displayed as down-pointing arrows. The best-fitting total SED is plotted in grey (thick), with the stellar component in red and the corresponding dust model in blue. The unattenuated (i.e. dust-free) model stellar SED is shown in green. The most uncertain area of the SED is the mid-infrared, which is constrained only weakly by the *IRAS* upper limits, with additional constraint coming from the energy balance criterion. The energy balance technique of dC10 enables us to only combine optical/NIR SEDs that are physically consistent with the sub-millimetre SED.

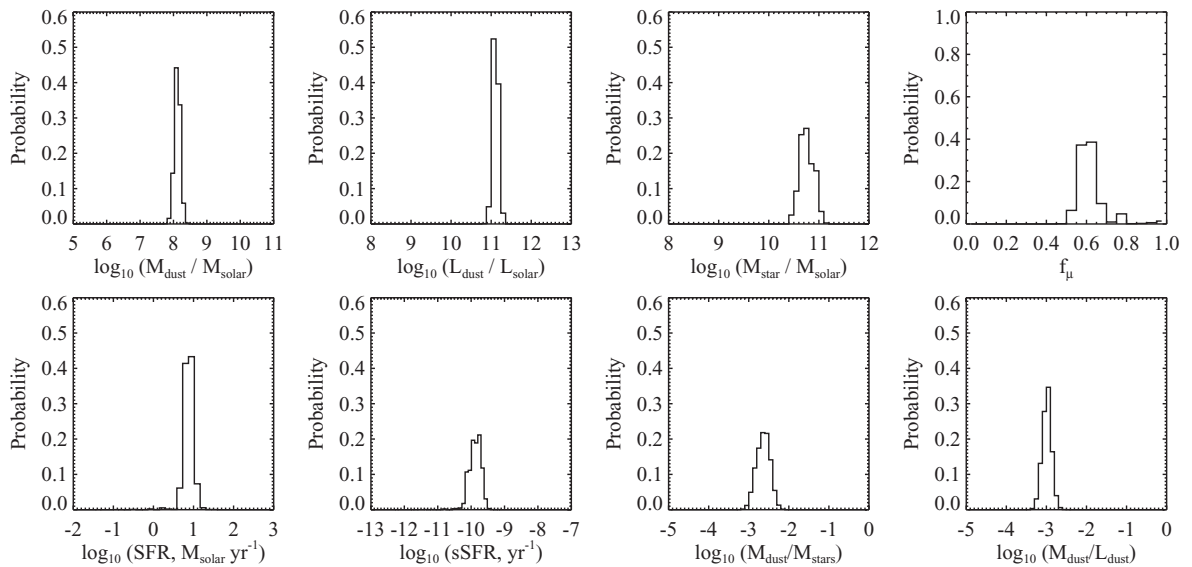


Figure 4. PDFs for the galaxy shown in Fig. 3 (H-ATLAS J090713.1-000322): the dust mass, dust luminosity, stellar mass, f_μ (the fraction of the total dust luminosity contributed by the diffuse ISM), the (specific) star formation rate, dust to stellar mass ratio and the ratio of dust mass to dust luminosity. Our results suggest that this galaxy is a massive luminous infrared galaxy (LIRG). Using these PDFs, we can estimate not only the median values for each parameter, but also the 16th and 84th percentiles, corresponding to the confidence range of our estimates.

mid-IR data, which are not available over the *H*-ATLAS SDP field at the time of writing.

4.1.1 Comparison with *IRAS*-selected samples

In Section 4.2, we compare the star formation activity and dust content of *H*-ATLAS 250 μm selected galaxies with those of a previous sample of local, star-forming galaxies selected at 60 μm with *IRAS* (dC10). To compare these two samples, we need to understand possible differences/biases in the derived physical parameters that may arise from the different selection of the samples. Therefore, in this section, we investigate the effects of including SPIRE data in

the SED fitting for a sub-sample of 250 μm selected galaxies for which we also have *IRAS* data. This allows us to assess whether any difference between our results and those of dC10 are due solely to the lack of SPIRE data for that study, or if they are rather due to effects of selection.

We take a sub-sample of the *H*-ATLAS 250 μm selected galaxies which are also detected by *IRAS* at 60 μm , and applied our fitting procedure twice; once including all available data, and a second time omitting all data longward of the PACS 100 μm band. The PACS 100 μm data were included for both sets of fitting to ensure that our results are as comparable as possible with dC10, since their galaxy sample was bright enough to be well detected with *IRAS* at 100 μm .

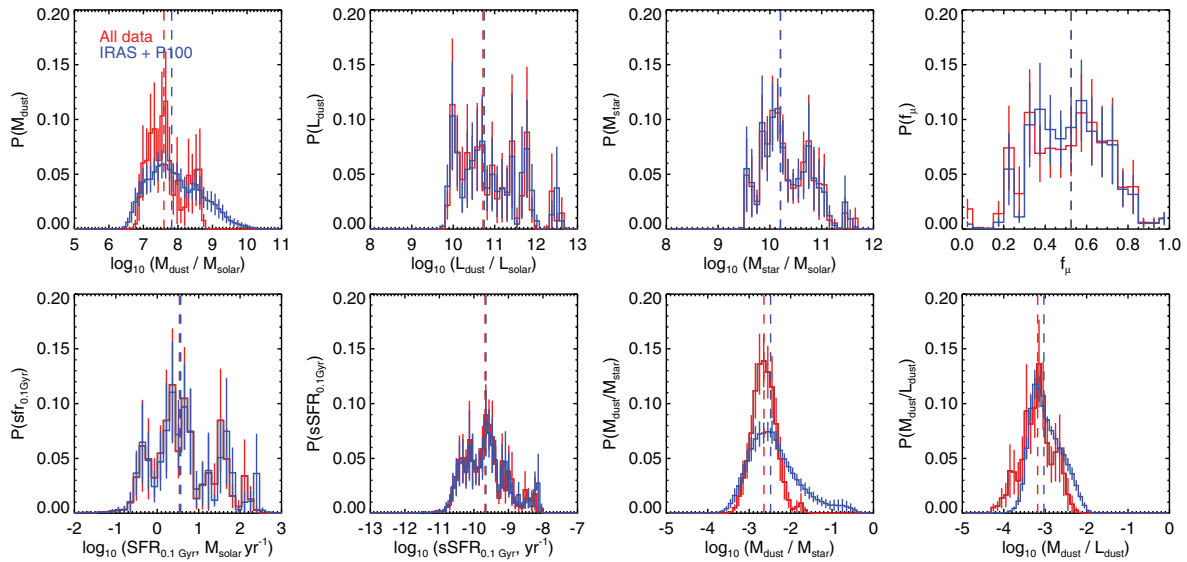


Figure 5. Stacked PDFs and errors for sources in our sample detected by *IRAS* at 60 μm , derived using the full *IRAS*, PACS and SPIRE data set (red histograms), and using only the *IRAS* 60 μm and PACS 100 μm data (blue histograms). The median values of each stacked PDF are indicated by the vertical dashed lines. The increased uncertainty in dust mass when the $\lambda > 100 \mu\text{m}$ data are not included in the fits is apparent in the wider range of values in the blue (i.e. no *Herschel* M_{dust} PDF. Stellar masses, f_{μ} , dust luminosity and star formation rates are much less strongly influenced by the inclusion of longer wavelength data, i.e. they are well constrained without data beyond 100 μm .

There are 18 *IRAS*-detected galaxies with aperture-matched *u*- to *K*-band photometry which are well described by our models. For these galaxies fitted both with and without the 160–500 μm data, we compare the medians of the stacked PDFs for a given parameter in each run. We estimate the uncertainty associated with each bin in a stacked PDF according to the 16th and 84th percentiles of the cumulative frequency distribution of values in each PDF bin (this method is discussed in greater detail in Appendix A). These stacked PDF comparisons and their associated uncertainties are displayed in Fig. 5, with the full data set PDFs shown in red and the *IRAS*-only results shown in blue.

In general, removing the $\lambda \geq 160 \mu\text{m}$ data from the SED fitting for those sources detected by *IRAS* results in small variations of the median values of the stacked PDFs for each population (dotted vertical lines in Fig. 5), but the changes are always less than the confidence interval derived according to the 16th and 84th percentiles of the stacked PDFs. The most noticeable effect of removing the $\lambda \geq 160 \mu\text{m}$ data is the considerably larger uncertainty in M_{dust} ; this is not surprising since the cold dust component dominates the total dust mass, and constraints on this component come primarily from the longer wavelength SPIRE data. There is a tendency for the model to overestimate the dust mass when using only *IRAS* data (see the tail to high M_{dust} values in Fig. 5), as the lack of SPIRE data allows the model to add in more cold dust without any strong constraint from the energy balance (since the contribution to the overall L_{dust} varies $\propto T^{4+\beta}$, warmer dust far outweighs colder dust in its effect on L_{dust}). The quantities $M_{\text{dust}}/L_{\text{dust}}$ and $M_{\text{dust}}/M_{\text{stars}}$ are much better constrained when including the longer wavelength data, for the same reasons discussed for the dust mass estimates above. The other parameters, L_{dust} , M_{stars} , SFR, sSFR and f_{μ} are all comparable in both samples.

4.1.2 The effect of lacking PACS observations

Whilst there are 1289 5 σ SPIRE sources with reliable optical counterparts in the *H*-ATLAS survey and good SED fits, we have 5 σ

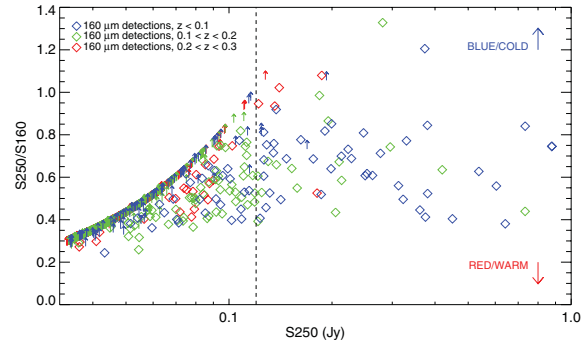


Figure 6. S_{250}/S_{160} colour as a function of 250 μm flux density, binned in redshift according to the colours as shown in the legend. At the fainter 250 μm fluxes, our PACS data detect only the warmer galaxies, as shown by the large number of lower limits on the S_{250}/S_{160} colour at these fluxes. At $S_{250} > 120 \text{ mJy}$, we sample the full range of colours (and therefore temperatures) in our 250 μm selected sample, so it is these galaxies that we use to study the impact of missing PACS data for the majority of our sources on the derived parameters. The vertical dashed line shows $S_{250} = 120 \text{ mJy}$, the 250 μm flux limit for the PACS-complete sub-sample.

PACS detections for only 207 and must rely on upper limits for the remaining sources. It is important to understand the effect of missing PACS data on our results, and so we now investigate the impact on our SED fits when we omit the PACS data for a sub-sample of PACS-detected galaxies drawn from our main sample. To determine a representative sample, we show in Fig. 6 the S_{250}/S_{160} colour as a function of 250 μm flux, binned in redshift. The PACS data are not deep enough to probe colder colours at fainter fluxes or higher redshifts, but do sample the full range of colours above $S_{250} \approx 120 \text{ mJy}$, at least for $z < 0.2$. To assess the impact of missing PACS data on the results of our SED fitting, we use these 59 sources with 160 μm PACS detections and $S_{250} \gtrsim 120 \text{ mJy}$ at $z < 0.2$, to check how the SED parameters change when the PACS data

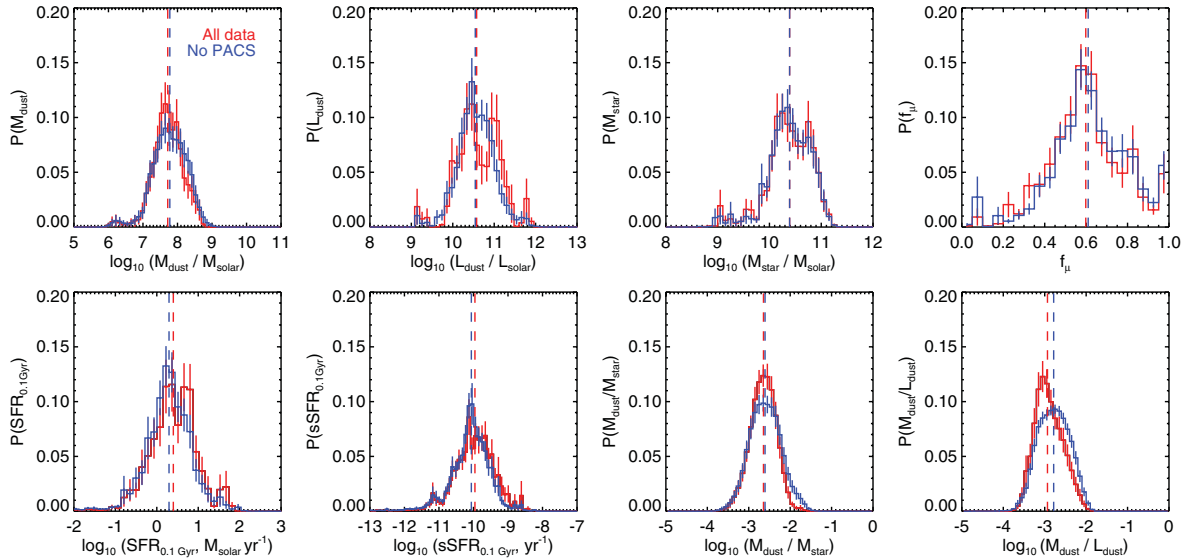


Figure 7. Stacked PDFs comparing the dust temperatures, dust mass and luminosity, stellar mass, f_{μ} , specific star formation rate, dust mass to luminosity ratio and dust to stellar mass ratio for the representative PACS-complete sub-sample. The results including all available data are shown by the red histograms, while those results derived neglecting the PACS data are shown in blue. The vertical dotted lines indicate the median values of the stacked PDFs. We find that fits lacking PACS data have sSFR underestimated by ~ 0.1 dex, and M_{dust} overestimated by ~ 0.06 dex. Estimates of the stellar mass and f_{μ} are largely unaffected by omitting the PACS data, while the effects on the $M_{\text{dust}}/L_{\text{dust}}$ and $M_{\text{dust}}/M_{\text{stars}}$ are consistent with the changes to their input parameters.

are removed from the fitting.³ We will refer to this sample as the ‘PACS-complete’ sample.

In Fig. 7, we show a comparison of the stacked PDFs when the PACS data are included and excluded from the fitting for the ‘PACS-complete’ sample. This is not quite the same effect which will apply to the full sample, as there we do have some PACS information (in the form of upper limits), while in this test we have no information when the PACS data are removed. This makes this comparison conservative, in the sense that the effects on the full sample are going to be no larger than the worst-case scenario we study here.

Removing the PACS information from the SED fitting causes the average estimate of the specific star formation rate to decrease by ~ 0.1 dex. Estimates of the stellar mass are, unsurprisingly, barely altered, while f_{μ} and L_{dust} are also robust in a sample average. Dust masses of the population are overestimated by approximately ~ 0.06 dex. The median offset for each parameter in the absence of PACS data is tabulated in Table 3.

Looking at the changes in globally averaged parameters in this way is reassuring; however, it is important to check that this is not masking a potential correlation of a bias in one parameter as a function of another. For example, we may overestimate M_{dust} at low values of L_{dust} and underestimate at high values – i.e. our estimates may be skewed – but still have an average offset consistent with zero bias. As we will next investigate trends of one parameter against others, and later bin SEDs by parameter, we must consider these effects now. We focus on these issues in detail in Appendix C, though to summarize, we find that the lack of PACS data does not introduce bias in any parameters as a function of redshift, M_{stars} or f_{μ} . The same is generally true of our estimated L_{dust} and M_{dust} , though these parameters possibly show weak correlations (i.e. they may be skewed). In the absence of PACS data, L_{dust} may be under-estimated

Table 3. The effects of omitting PACS data from the SED fitting results for those sources in the ‘PACS-complete’ sample. These offsets are also shown in Fig. 7. Note that all values are consistent within the uncertainties derived from the 16th and 84th percentiles of the stacked PDFs. Furthermore, and as can be seen in Fig. C1 of Appendix C, the offsets for individual galaxies are almost always consistent with zero once the errors are taken into account.

Parameter	Offset (Best – no PACS)
$\log_{10} L_{\text{dust}}$	0.03 dex
$\log_{10} M_{\text{dust}}$	-0.06 dex
$\log_{10} M_{\text{stars}}$	0.00 dex
f_{μ}	-0.01
sSFR	-0.10 dex
SFR	-0.10 dex
$M_{\text{dust}}/L_{\text{dust}}$	-0.15 dex
$M_{\text{dust}}/M_{\text{stars}}$	-0.04 dex

at large M_{dust} , and overestimated towards lower dust masses, though the offset averaged over the whole population is small. M_{dust} shows weak bias with $M_{\text{dust}}^{\text{noPACS}}$; in that our PACS-free estimates of M_{dust} are slightly high for large M_{dust} , though the correlation shows considerable scatter and the overall offset across all values is small. Our estimates of SFR and sSFR show larger scatter than the other parameters, reflected in the larger error bars on $\Delta(s)\text{SFR}$, though it is difficult to discern any skewed bias in the derived values. We will discuss the impact of possible bias with these parameters later in this paper.

It is worth noting that because of the good multi-wavelength coverage and lack of temperature/colour bias in the $S_{250} > 120$ mJy PACS-complete sample (Fig. 6), we can use it to determine our best estimate of the dust temperature in low-redshift $250 \mu\text{m}$ selected galaxies. We determine a median likelihood estimate of $T_{\text{cold}} = 20.4 \pm 0.4$ K from the DCE08 model and an isothermal

³ The equivalent sample for the PACS $100 \mu\text{m}$ channel, which requires $S_{250} \gtrsim 200$ mJy, contains no additional sources above those selected here.

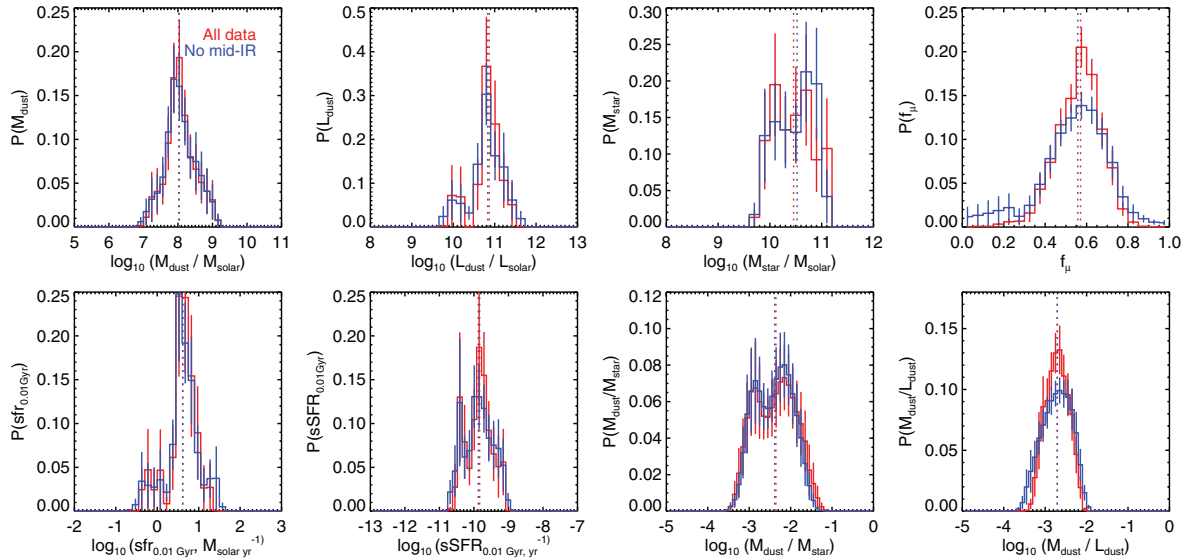


Figure 8. A comparison between the stacked PDFs derived by fitting 14 galaxies selected from the *BLAST* survey of the E-CDFS. In red, we show histograms of the results obtained when the mid-infrared data (i.e. those at 3.6–8.0, 24 and 70 μm) are included in the fitting, whilst the blue histograms show the results in the absence of these data. The similarity of these two sets of PDFs indicates that our estimates of these parameters are not biased by the absence of mid-infrared coverage in our data set, and consequently that the absence of such data does not limit the validity of our results. Once more, the median values of the PDFs are indicated by the vertical dotted lines.

value from simple grey-body fitting to the FIR data of $T_{\text{grey}} = 26.1 \pm 3.5 \text{ K}$ (assuming $\beta = 1.5$ for comparison with literature values). These estimates are colder than values in the literature predating *Herschel*; for example, SLUGS found $T_{\text{grey}} = 36 \pm 5 \text{ K}$, $\beta = 1.3$, for the *IRAS*-selected sample (Dunne et al. 2000) and $T_{\text{grey}} = 31.6 \pm 0.6 \text{ K}$ for the optically selected sample (Vlahakis et al. 2005). Our temperatures are comparable to those observed in galaxy samples selected at longer wavelengths but including data from 24 to 160 μm using e.g. *BLAST* ($26 \pm 5 \text{ K}$, $\beta = 1.5$, Dye et al. 2009) or selected in the *K* band and observed with *Herschel* (e.g. $T_{\text{grey}} \approx 20 \text{ K}$, $\beta = 2.0$, Boselli et al. 2010; $T_{\text{grey}} \approx 25.8 \text{ K}$ for spirals in Skibba et al. 2011; or $\approx 23 \text{ K}$, $\beta \approx 1.5$, Dale et al. 2012). Multiple-component modified blackbody SED fits have long noted the presence of substantial cold dust components with lower temperatures, consistent with our findings (e.g. Dunne & Eales 2001; Contursi et al. 2001; Vlahakis et al. 2005; Clements, Dunne & Eales 2010; Rowan-Robinson et al. 2010; Galametz et al. 2011, Planck Collaboration 2011).

4.1.3 The effect of missing mid-IR observations

At the time of writing, mid-infrared data over the *H-ATLAS* fields are unavailable [the first public data release of the Wide-Field Infrared Survey Explorer – *WISE* (Wright et al. 2010) – survey does not include the *H-ATLAS* SDP field], we investigate the effects of not having such data on the PDFs by applying the same fitting procedure to a sample of galaxies selected at 250 μm in data from the Balloon-borne Large Aperture Sub-millimetre Telescope (*BLAST*; Devlin et al. 2009). We derive multi-wavelength SEDs and PDFs for a sample of 14 *BLAST* galaxies in the Extended *Chandra* Deep Field South (E-CDFS; Lehmer et al. 2005) which have $\geq 5\sigma$ detections in all three *BLAST* bands (250, 300, 500 μm ; Dye et al. 2009) and spectroscopic redshifts from Eales et al. (2009), with additional photometry in the *GALEX* (FUV and NUV – Morrissey et al. 2007), optical (*ugriz*), 2MASS *J* and *K_s* (Skrutskie et al. 2006), MIR (3.6–

8.0, 24, 70 μm), as well as FIR (160 μm) bands from the *Spitzer Space Telescope* (Lonsdale et al. 2003).

In Fig. 8, we show the stacked PDFs for the same parameters as in Fig. 7 derived for these *BLAST* galaxies. The red histograms show the PDFs determined when we include the complete data set, while the blue histograms show the PDFs derived in the absence of the mid-infrared data. The similarity between these two sets of histograms, and the absence of bias between them, suggests that our estimates of the dust mass, luminosity and SFR are robust to the absence of mid-infrared data in our wider *H-ATLAS* data set, although these tests have necessarily only been applied for a small number of sources. The mid-IR accounts for only a small fraction of the total infrared emission, and the similarity of the PDFs highlights the power of the energy balance criterion in constraining the dust luminosity even in the absence of mid-infrared data. The detailed shape of the SED in the mid-IR is clearly not well defined for our sample and constraints on this can only come from comparison with mid-IR data, e.g. from *WISE*.

4.2 The properties of sub-millimetre selected galaxies in *H-ATLAS*

4.2.1 First results and comparison with previous studies

By stacking the PDFs for galaxies well described by our model, we determine a median dust luminosity for our whole sample of $5.6 \times 10^{10} L_{\odot}$, placing the average *H-ATLAS* galaxy’s luminosity just below what would traditionally have been considered a LIRG. Fig. 9 shows the dust luminosity as a function of redshift for *H-ATLAS* (red) and it is important to note that *H-ATLAS* traces typical star-forming spirals (with $\log L_{\text{dust}} < 11.0 L_{\odot}$) out to much higher redshifts ($z \sim 0.35$) than was possible with *IRAS* ($z < 0.05$). Our SED-fitting results indicate that the star formation rate of the average low-redshift *H-ATLAS* galaxy is $\sim 3.4 M_{\odot} \text{ yr}^{-1}$, and that the median dust to stellar mass ratio is ~ 0.4 per cent.

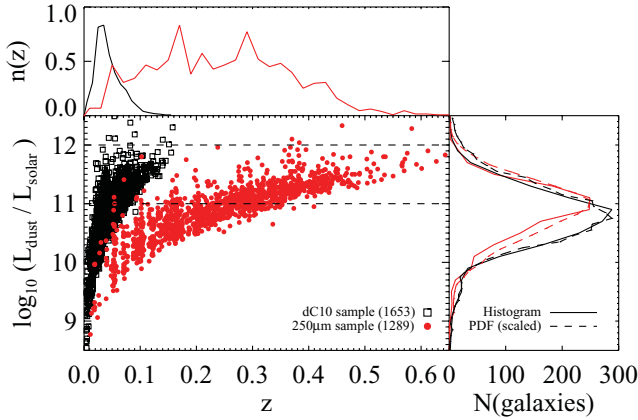


Figure 9. The dust luminosity of *Herschel*-ATLAS-selected galaxies with reliable counterparts, and reliable SED fits to our compiled photometry, as a function of redshift, is shown in red. The median redshift is $\bar{z} = 0.239$ and the median dust luminosity of our full sample is $5.6 \times 10^{10} L_{\odot}$. We also include data points from dC10 for comparison, in black, highlighting the different redshift and luminosity properties of each sample. The horizontal dashed lines delineate those galaxies with luminosities in the LIRG and ULIRG categories, at 10^{11} and $10^{12} L_{\odot}$, respectively. We also show histograms detailing the redshift distribution of each sample (top), in which the relative heights of the two histograms are arbitrary to bring out the contrasting properties of the two samples. On the right, we show that the dust luminosity distributions for the two samples are comparable.

In Fig. 10, we present histograms of the results of our SED fitting, and those from dC10, who applied the same method to a *GALEX*-SDSS-2MASS-*IRAS* data set and included photometry only up to $100 \mu\text{m}$. The different selection criteria of the dC10 sample produces a different redshift distribution from the *H*-ATLAS sample; however, the stellar mass and dust luminosity distributions are similar, and a comparison of specific parameters can still be

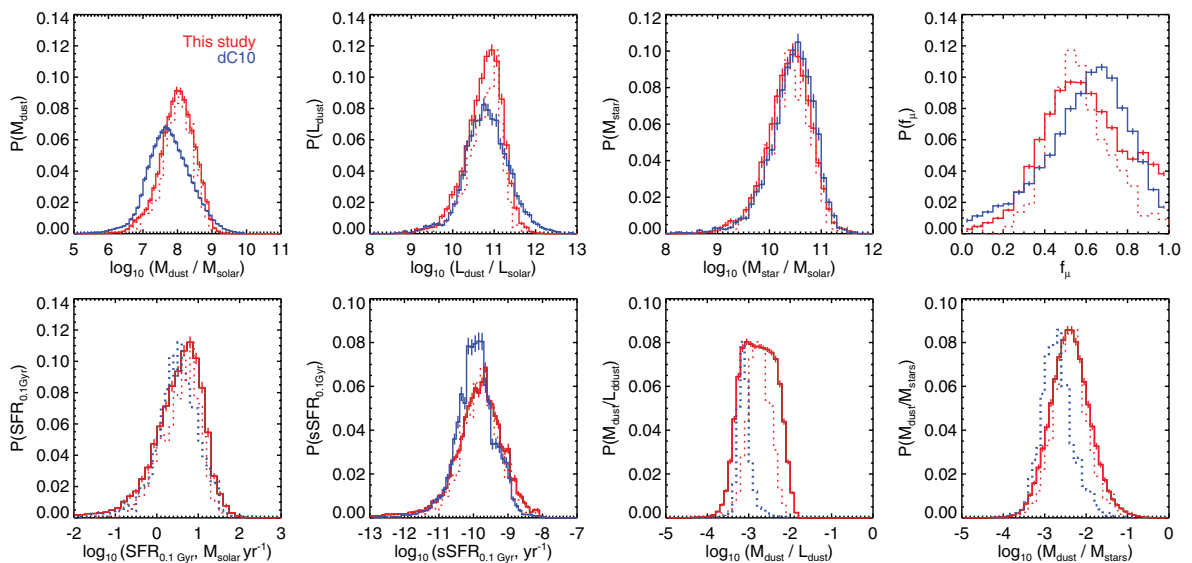


Figure 10. Comparisons of the stacked PDFs from *H*-ATLAS SED fitting (red histograms) with those of dC10 (blue histograms). The red dotted histograms indicate the distribution of the median likelihood values for *H*-ATLAS (i.e. the 50th percentiles of the individual PDFs, arbitrarily renormalized for ease of comparison), which are narrower than the stacked PDFs since they do not reflect the uncertainty in the derived values. The histograms compare parameter distributions for the $z < 0.35$ sample which are well described by our model, with the results of dC10. We note that the dC10 results do not include PDFs for SFR, $M_{\text{dust}}/L_{\text{dust}}$ or $M_{\text{dust}}/M_{\text{stars}}$, and so we include the quotient of the median values of the relevant PDFs for the dC10 sample shown as thick blue dotted histograms. The stacked results suggest that galaxies selected in *H*-ATLAS contain on average a factor ~ 2 more dust than those galaxies in the dC10 sample, although the luminosities are broadly comparable.

Table 4. Comparison between the median properties of the dC10 *IRAS*-selected sample and the *H*-ATLAS $250 \mu\text{m}$ selected sample.

Parameter	Median values	
	dC10 $z < 0.16$	$250 \mu\text{m}$ $z < 0.35$
SFR ($M_{\odot} \text{ yr}^{-1}$)	3.25 \dagger	4.17 \dagger
$\log \text{ sSFR} (\text{ yr}^{-1})$	-9.94	-9.80
$\log M_{\text{stars}} (M_{\odot})$	10.48	10.40
$\log M_{\text{dust}} (M_{\odot})$	7.74	8.01
$\log L_{\text{dust}} (L_{\odot})$	10.81	10.81
$\log (M_{\text{dust}}/L_{\text{dust}})$	-3.12 \dagger	-2.77 \dagger
$\log (M_{\text{dust}}/M_{\text{stars}})$	-2.72 \dagger	-2.38 \dagger
f_{μ}	0.62	0.57
N (galaxies)	1653	1032

instructive. In Table 4, we provide results for the dC10 sample ($z < 0.16$) and for our sample of $250 \mu\text{m}$ selected galaxies (limited to $z < 0.35$).

On average, the galaxies selected at $250 \mu\text{m}$ have slightly higher specific star formation rates than those in dC10, by $\log_{10} \text{ sSFR} \approx 0.1$ dex. Though the dust luminosities and stellar masses are roughly the same, the dust masses in the two samples differ by 0.3 dex, with the *H*-ATLAS galaxies being more dusty. This translates into higher ‘specific’ dust masses for *H*-ATLAS galaxies (higher $M_{\text{dust}}/L_{\text{dust}}$ and $M_{\text{dust}}/M_{\text{stars}}$). Part of this difference is due to the evolution in dust masses with redshift (Dunne et al. 2011), as the *H*-ATLAS sample probes a higher redshift range. However, this is not the whole story as we will discuss in the next section.

In Fig. 10, we compare the stacked PDFs of several physical parameters for the *IRAS*-selected sample of dC10 (blue) and the *H*-ATLAS $250 \mu\text{m}$ selected sample (red). The dC10 distribution

of $M_{\text{dust}}/L_{\text{dust}}$ values is considerably narrower than that based on the results of this study. This may be because *Herschel*'s selection at $250\ \mu\text{m}$ is intrinsically more sensitive to a range of $M_{\text{dust}}/L_{\text{dust}}$ values, as it is not solely sensitive to the warmer dust but also picks up the cold, dusty galaxies which have large $M_{\text{dust}}/L_{\text{dust}}$ but are not necessarily warm enough for *IRAS* to detect.

4.2.2 Star formation and dust in $250\ \mu\text{m}$ selected galaxies

We now explore the star formation activity and dust properties of *H-ATLAS* galaxies. In Fig. 11, we plot relationships for three different galaxy samples: the results of this study (left), and the dC10/DCE08 samples (right, orange and blue squares, respectively). Each individual galaxy is shown in grey, and we split our sample in bins of redshift, with colours as shown in the legend. The positions of the error bars correspond to the mean of the galaxies in that redshift bin, while the size of the error bar represents the standard deviation of the derived values within that redshift bin. The best-fitting relation

between SFR and dust mass from dC10 (dashed line) appears to trace the low dust-mass edge of the $250\ \mu\text{m}$ selected population. The slope of the relationship for *H-ATLAS* appears to be the same, but the *H-ATLAS* sources are offset such that they have larger dust masses for a given SFR compared to *IRAS* selected galaxies.

It is unlikely that this offset is a result of biases in the fitting given the difference in FIR coverage for the two samples. As we showed in Section 4.1.1 for the *IRAS* sample, we do not expect M_{dust} to be underestimated (if anything, the converse applies) due to the lack of data at wavelengths longer than $100\ \mu\text{m}$. For *H-ATLAS* sources without PACS data, there was a small tendency to overestimate the dust mass at the highest values of SFR, but not at a level which could explain this offset which is present at all SFR values. This effect is also not due to redshift differences between the two samples, as the error bars show; increasing redshift drives a given galaxy along the plotted slope and not away from it. Comparing only sources within the same redshift range (i.e. if we limit the *H-ATLAS* results to $z < 0.16$), we still find an increase in dust mass per unit star

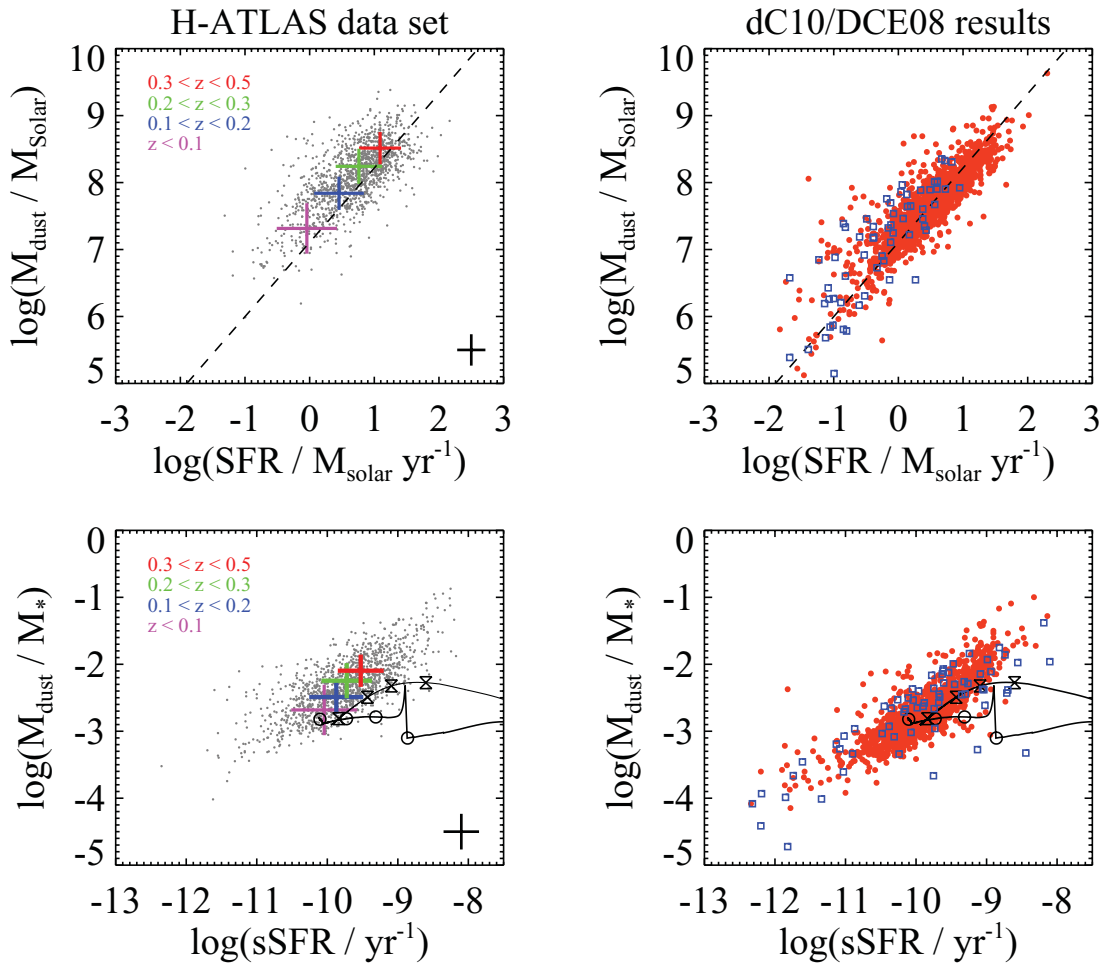


Figure 11. Comparisons between *H-ATLAS* $250\ \mu\text{m}$ selected galaxies and other local galaxy surveys. Top row: the variation of the total dust mass as a function of the star formation rate for the three samples of galaxies; on the left, we show the *H-ATLAS* $250\ \mu\text{m}$ selected sample with at least two far-IR detections in our data set in grey. The coloured error bars indicate the mean positions of those galaxies in the redshift range shown by the colours, with size equal to the standard deviation of the values in each bin. On the right, we present the same results for the *GALEX*–*SDSS*–*2MASS*–*IRAS* sample from dC10 in orange circles, with the *SINGS* galaxy sample from dC08 in blue squares. Overplotted in each frame is the best-fitting relationship from dC10, which is offset with respect to the results of our best-fitting SEDs. Bottom row: the ratio of dust mass to stellar mass as a function of specific star formation rate, with the same colour scheme as above. The ‘solar-neighbourhood’ and ‘dwarf-irregular galaxy’ theoretical models of Calura, Pipino & Metteucci (2008) are overplotted as the open circles and the open bow-ties, respectively, with the symbols indicating the locations of the models at ages of 1, 3, 6 and 12 Gyr. The models are described in considerable detail in the main text, and the majority of *H-ATLAS* sources do not overlap with the locus of theoretical points.

formation rate for the *H*-ATLAS sample, relative to the DCE08 and dC10 samples. At low values of dust mass, the *H*-ATLAS sample includes few sources with $\log_{10}(M_{\text{dust}}/M_{\odot}) < 6.5$. This is due to the flux limit in *H*-ATLAS combined with the small survey area in SDP. The ‘missing *H*-ATLAS sources’ following the *IRAS* and Spitzer Infrared Nearby Galaxy Survey (SINGS; Kennicutt et al. 2003) points at the lower left of the plot are simply below the detection threshold of the *H*-ATLAS SDP sample.

The lack of *IRAS* sources with high $M_{\text{dust}}/\text{SFR}$ may reflect the lack of sensitivity of *IRAS* to cold dust; galaxies with low SFR and larger masses of dust would tend to have colder dust temperatures and therefore be absent from *IRAS* selected samples. This comparison suggests that *IRAS* preferentially selects those galaxies with the highest SFR per unit mass of dust, since more star formation for a given mass of dust will result in stronger dust heating and more emission at the *IRAS* selection wavelength of 60 μm . For the DCE08 SINGS sample (squares), which are not selected from a flux-limited FIR survey, the trend is similar to that seen in *H*-ATLAS but extended to lower values of dust mass.

In the bottom panel of Fig. 11, we also plot the ratio of the dust to stellar mass as a function of specific star formation rate. This relationship was first noted by dC10, and their data are plotted in the right-hand panel of Fig. 11. Compared to the sample in dC10, the *H*-ATLAS galaxies appear to have higher specific dust content (relative to stellar mass) for a given specific star formation rate. The reason for this difference is likely to be the same as that in the upper relationship between M_{dust} and SFR since the stellar mass distributions of the two samples are very similar.

We overlay the predictions of dust evolution tracks from the chemical evolution models of Calura et al. (2008), which are based on the model in Dwek (1998) and follow the build-up of heavy elements and dust formed in low- and intermediate-mass stars (LIMS) during their asymptotic giant branch phase and in both Type Ia and Type II supernovae. The upper black curve shows the evolution of dust from a dwarf-irregular galaxy with continuous star formation. The solar-neighbourhood model, which reproduces the properties of the Galactic disc and centre (see Calura et al. for more details), is indicated by the lower curve. As discussed in dC10, the observed trend between specific dust mass and specific star formation rate can be explained as follows: dust is produced through stellar sources; its production rate is closely linked to the star formation rate and rises steadily as the galaxy starts to build up stellar mass. As gas is consumed, the star formation rate declines and so less dust is formed. Given the destruction of dust via astration, outflows and supernova shocks, at this stage, galaxies can no longer replenish their dust content through star formation and the dust mass decreases. The chemical evolution models trace the evolutionary history of the galaxy; increasing the star formation rate, the gas mass available to form stars and/or the amount of dust from supernovae will drive the models towards the upper right in Fig. 11, i.e. towards those *H*-ATLAS galaxies with the highest specific dust masses.

The dust mass evolution as traced by the Calura/Dwek chemical evolution models is likely to be a best-case scenario since their assumed condensation of dust required from the heavy elements ejected by LIMS during their stellar wind phases and/or massive star supernovae is rather optimistic compared to the dust masses observed for stellar sources (e.g. Morgan & Edmunds 2003). Indeed, Dunne et al. (2011) find it extremely difficult to explain those galaxies with the highest dust masses in the *H*-ATLAS sample without grain growth in the ISM as the main contributor to the interstellar dust budget, or a top-heavy IMF (see also Gomez et al., in preparation).

We now investigate whether the dust and star formation properties of our sample vary as a function of stellar mass. In Fig. 12 we show the variation of $M_{\text{dust}}/M_{\text{stars}}$, $M_{\text{dust}}/\text{SFR}$ and f_{μ} as a function of specific star formation rate binned by stellar mass, such that each bin has approximately equal numbers of galaxies. In the upper and right panels, we plot histograms for each of the bins in stellar mass, with the median values overlaid as vertical/horizontal lines. The lower stellar mass galaxies have higher specific dust mass; a similar trend is also observed in stacking analyses of optically selected galaxies in the *H*-ATLAS SPIRE data (Bourne et al. 2012) and also in volume-limited samples of very local galaxies (e.g. Cortese et al. 2012), suggesting that this effect is not the result of selection bias in our data.

It is also clear that the lower mass galaxies are considerably more actively star-forming than the high-mass galaxies, consistent with the idea that the massive galaxies have consumed more of their available baryonic fuel through either the process of star formation or the aftermath of AGN feedback than their less massive neighbours (e.g. Cowie et al. 1996; Bundy et al. 2006, 2009; Hopkins et al. 2007; Pozzetti et al. 2010).

The lower panel of Fig. 12 suggests that lower mass galaxies have smaller contributions to their total infrared luminosity from dust in the ambient ISM, than their more massive counterparts (lower f_{μ}). This, once more, is due to the fact that the less massive galaxies are undergoing proportionally more star formation and so the stellar birth clouds make a larger contribution to the total FIR energy output.

As in dC10, we observe a small fraction of low-mass galaxies with high specific star formation rates and high f_{μ} . The value of f_{μ} in the model enters both in the optical part of the star formation history libraries (based on the age of the stellar population and opacity of the birth clouds) and from the combination of the dust components. Clearly, there are degeneracies in the IR part of the SED; for example, a high f_{μ} with a warm temperature for the ISM component could produce a very similar looking FIR SED to a lower f_{μ} with a cool temperature for the birth cloud component. However, the optical colours for these two scenarios may look different as a result of the different stellar ages and attenuations in the model and so the IR data are not the only (or even the strongest) constraint on this parameter.

The high f_{μ} values indicate that dust in the diffuse ISM heated by stars older than 10 Myr dominates the FIR emission in these sources, but the high sSFR averaged over the last 0.1 Gyr suggests that these sources have very recent star formation activity. If we instead use the sSFR values averaged over the last 10 Myr, these galaxies are assigned more modest values of sSFR and shift to the left suggesting that the models which best fit the data are ones in which the star formation was recently truncated. These sources are all strong emission line objects, not displaying classical ‘post-starburst’ spectra and so the high f_{μ} and sensitivity of model sSFR to the time-scale of integration could indicate that they are in a short-lived phase transitioning from their obscured birth clouds to the more diffuse ISM. If global SED fitting can potentially isolate sources in specific stages of evolution, this could be a powerful technique; however, full testing on a larger sample including a detailed analysis of the optical spectra is required in order to confirm this.

4.3 Variation of SEDs within the 250 μm galaxy population

We now analyse the shape of the averaged population SEDs as a function of model parameter, in order to understand the main

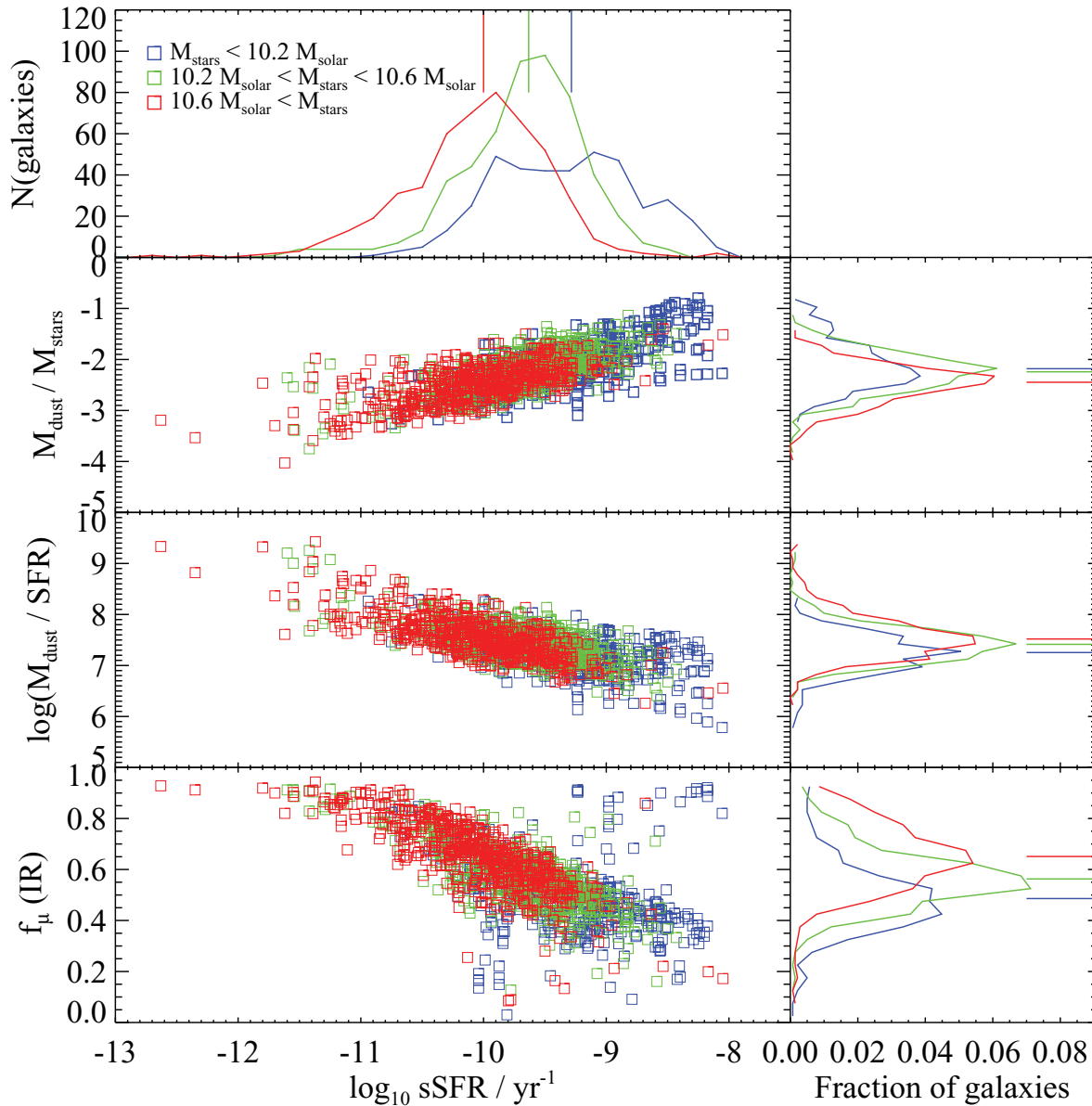


Figure 12. The variation of the dust to stellar mass ratio, dust mass per unit star formation rate and the f_{μ} parameter as a function of specific star formation rate derived from our SED fitting. The galaxies are additionally binned into three populations based on their stellar mass, with the low-, intermediate- and high-mass galaxies (with limits of $\log_{10}(M/M_{\odot}) < 10.2$, $10.2-10.6$ and > 10.6), shown by the blue, green and red squares, respectively. To the right of each panel, we also show histograms corresponding to that mass bin's distribution relative to the vertical axis, and in the very top panel we show histograms of the specific star formation rate in each mass bin.

physical properties driving the shape of galaxy SEDs. We obtain median SED templates by stacking the SEDs of our galaxies according to their best-fitting parameters, following the method described in detail in Appendix D.

In Fig. 13, we show the median SEDs in stacks binned on (a) specific star formation rate, (b) dust luminosity, (c) stellar mass and (d) redshift. We include only galaxies at $z < 0.35$ in this analysis, i.e. we only consider the range in redshifts where we believe that our sample is representative. We also show the unattenuated starlight SED in the same bins in Fig. 14 to illustrate changes in the underlying stellar populations fitted by the models.

As a further check of the influence of having PACS detections for only a fraction of our sources, we have performed the stacking in each bin twice: once including all available data in the fitting (solid

lines) and once omitting the PACS data for all sources (dotted lines). The number of sources in each stack is shown in the legend to each sub-figure, as is the fraction of these with 5σ PACS detections. The broad similarity between the solid and dotted stacked SEDs – i.e. those including and neglecting the PACS data – is generally reassuring; we now discuss each set of stacked SEDs in detail.

4.3.1 Specific star formation rate

The most striking trends are with specific star formation rate, shown in Fig. 13(a) and Fig. 14(a); those galaxies with the highest specific star formation rates not only have the youngest stellar populations, but also the hottest effective dust temperatures manifest by the bluer

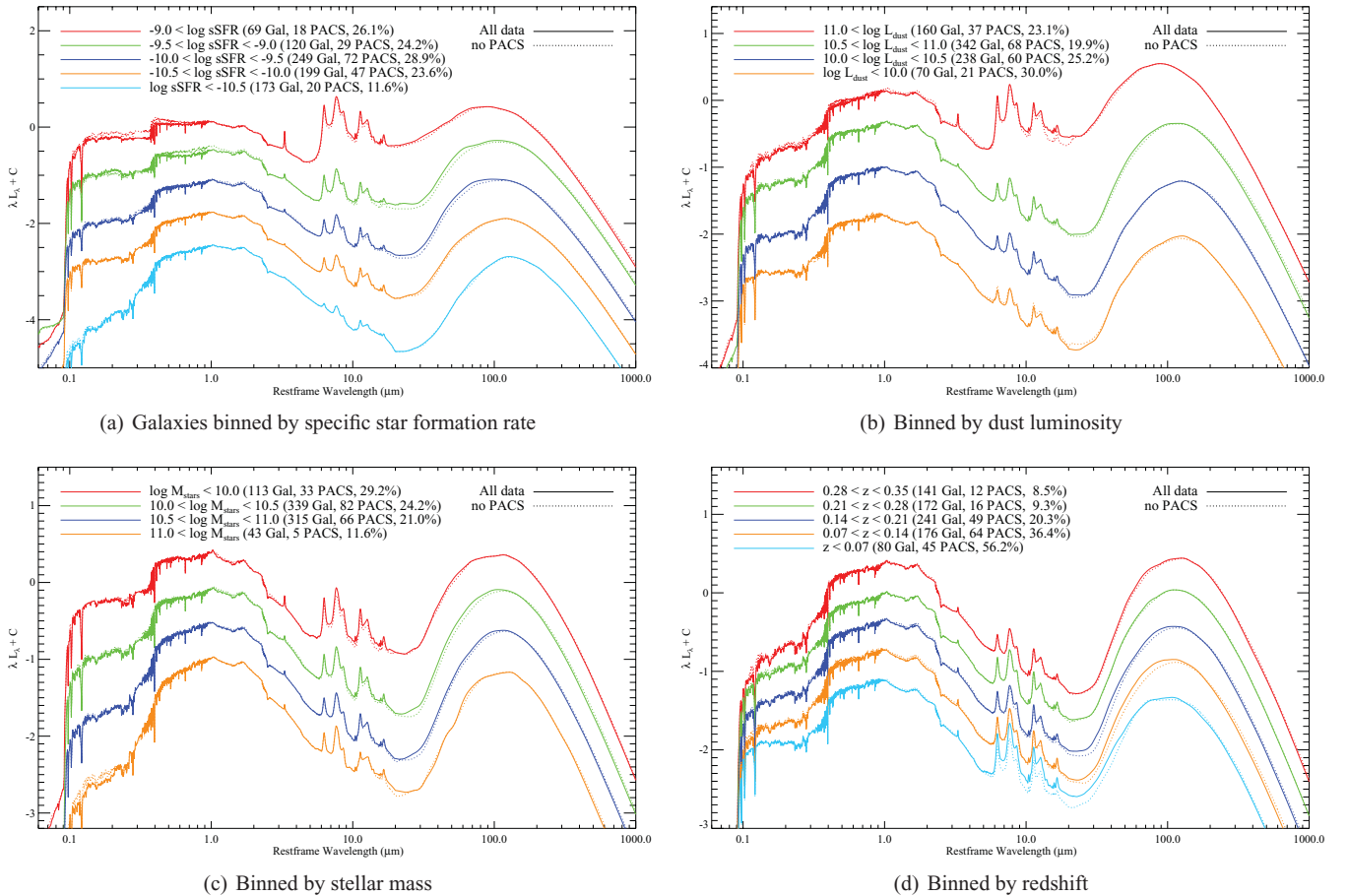


Figure 13. The variation in the SEDs of $250\ \mu\text{m}$ selected galaxies in bins of their (a) specific star formation rates, (b) dust luminosity (c) stellar mass and (d) redshift. The range of values for each bin and the number of galaxies in each bin are as described in the legend for that particular plot. These median galaxy SEDs have been normalized to their mean flux between 0.2 and $500\ \mu\text{m}$, and offset from one another so as to reveal the different properties of each median SED. Whilst the vertical position of each galaxy is arbitrary, the morphology of each median SED is not. The differing specific star formation rates (with increasing specific star formation rates from the bottom of the plot upwards) are apparent in the dust properties of these median spectra in the FIR wavelengths; the most vigorously star-forming galaxies have warmer dust temperatures due to the extra source of heating in the form of a recent yield of OB stars. The specific star formation rate appears to be the key driver of the properties of a $250\ \mu\text{m}$ selected galaxy’s SED, whereas the variation between different bins of other properties is weaker. The stacked SEDs constructed omitting the PACS data are shown by the dotted lines, whilst those derived using all available data are shown as the solid lines.

optical colours and shorter peak wavelengths of the FIR bump, respectively. Similar results were also found by DCE08 for the much smaller sample of SINGS galaxies.

4.3.2 Total dust luminosity

In Fig. 13(b), we show the relatively weak variation of the SED properties in our sample as a function of dust luminosity. The UV–optical part of the transmitted SED is similar in all but the highest L_{dust} bin, which as shown in Fig. 14 is dominated by a younger intrinsic SED with greater reddening than the less luminous bins. The template PAH luminosity increases markedly with L_{dust} though this area of the SED is only indirectly constrained by the model priors and energy balance (due to the absence of mid-infrared observations in this study) and so we cannot determine how significant this is. The FIR/optical ratio increases with L_{dust} , indicating that galaxies with higher L_{dust} are also more obscured with a greater fraction of their bolometric luminosity being re-radiated by dust. The shape of the FIR peak seems to be largely uncorrelated with L_{dust} until the highest bin, when it shifts to the blue; thus, the most luminous dust

sources have warmer temperatures, but it does not appear to be a monotonic trend across the range of L_{dust} probed. This change in the peak wavelength is however consistent with the differing intrinsic (i.e. unattenuated) starlight SEDs shown in Fig. 14; it is clear that the more dominant young stellar population in the most luminous bin of L_{dust} is associated with the apparently hotter dust template in the same bin.

At this point, we need to proceed with caution in our conclusions because of the potential bias in L_{dust} when PACS data are missing (as discussed in Section 4.1.2 and Appendix C). The legend in Fig. 13 shows the fraction of PACS-detected sources in each bin, and also shows by dotted lines the same stacked template SEDs compiled when the PACS data are neglected from the fitting (i.e. even for those galaxies which are detected by PACS). As Fig. 13(b) shows, the fraction of PACS-detected sources in each template bin of L_{dust} is approximately constant, and the results do not change when the PACS data are neglected altogether; this suggests that they are robust to the presence/absence of PACS data. The number of sources in a stack in L_{dust} is almost always in the minority, however, which could also be the root cause of the similarity between the PACS

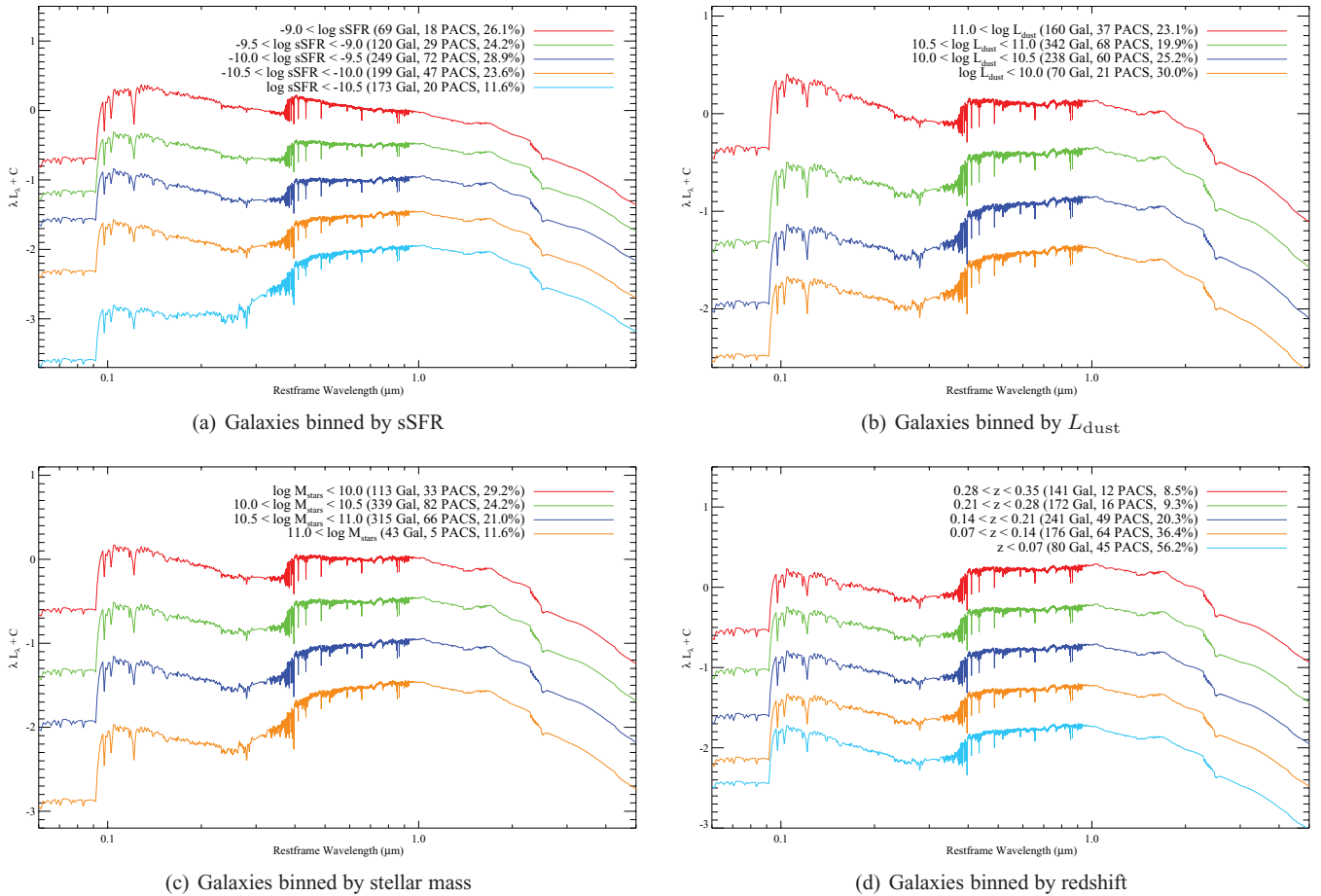


Figure 14. Stacked best-fitted unattenuated (i.e. intrinsic) stellar SEDs, derived in the same $z < 0.35$ bins of (a) sSFR, (b) L_{dust} (c) M_{stars} and (d) redshift as for the full panchromatic SEDs in Figs 13. The colours are identical to Figs 13(a)–(d), and each stack has been derived including all available data; once more, the normalization of each SED is arbitrary, but the morphology is not.

and no-PACS stacks. To check that this is not the case, we applied our stacking analysis to the PACS-complete sample, dividing it into two luminosity bins containing approximately equal numbers of galaxies and stacking the best-fitting SEDs derived in the two bins of L_{dust} , both including and excluding the PACS data. Fig. 15 shows the results for the most/least luminous sources in the top/bottom panel, including the PACS data (in red) and neglecting them (in blue), with each stack normalized at $250 \mu\text{m}$. At lower luminosities, the lack of PACS data has no effect on the stacked FIR SED shape and so for bins below $\log_{10}(L_{\text{dust}}/L_{\odot}) < 10.5$, we can be confident that the lack of trend of SED morphology with L_{dust} is robust. For the bin with $\log_{10}(L_{\text{dust}}/L_{\odot}) > 10.5$, there is more luminosity in the mid-IR and PAH component when PACS data are included compared to when they are not, but this is an area of the SED which we cannot confidently discuss with the present data set. The FIR peak is broadened when the PACS data are included, but not shifted significantly, while the optical/FIR ratios are consistent, and the median optical templates are almost identical. We do observe an increase in the range of values (i.e. the bounds of the 16th and 84th percentiles) seen at optical wavelengths derived in the absence of PACS data, though they are broadly consistent. Indeed, these stacked SEDs are compiled from smaller numbers of input galaxies than any of the individual stacked SEDs in Fig. 13, and so the stacked median SEDs in Fig. 15 (and their percentiles, dotted) in particular are more susceptible to the influence of small numbers at all wavelengths than those in our wider study.

4.3.3 Stellar mass

In Fig. 13(c) we show the variation of the galaxies in our sample as a function of their stellar mass. Unsurprisingly, the most massive sub-sample has a considerably more dominant old stellar population in the optical wavelengths than the least massive sub-set, consistent with the unattenuated stellar SEDs stacked in the same way in Fig. 14(c). The lowest mass galaxies have broader FIR peaks, suggesting they have a larger warm dust component than the larger stellar mass sources. They also have stronger PAH emission in the templates, but again we caution that this is not constrained by data for this sample. This shift in the FIR SED shape with mass is likely due to the lower mass galaxies having the highest sSFR (i.e. ‘downsizing’, as previously discussed) and consequently their average SED shows more of a warm component heated by the ongoing star formation.

4.3.4 Redshift

Finally, we note the weak variation in the FIR SEDs of these galaxies when binned by redshift, with the panchromatic stacks shown in Fig. 13(d) and the unattenuated stellar component in Fig. 14(d). The FIR SEDs of these populations all have similar temperatures, with the main difference between them being among their optical colours, with the higher redshift stacks appearing redder. Fig. 14(d) shows that the intrinsic stellar populations in each bin are very

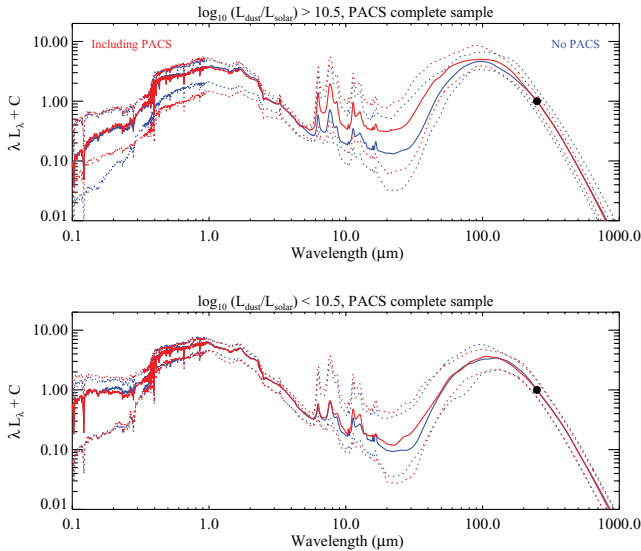


Figure 15. Stacked SEDs in two bins of L_{dust} derived using the PACS-complete sample. The top panel shows the stacks of those galaxies with high luminosity ($\log_{10}(L_{\text{dust}}/L_{\odot}) > 10.5$), while the bottom panel shows the stack for the lower L_{dust} galaxies. The boundary values are chosen so as to have approximately equal numbers of galaxies in each bin, with the galaxies assigned to one bin or the other according to the L_{dust} estimate derived using the same set of data (i.e. including/neglecting the PACS data). In each panel, we show the stacked SEDs (solid) and 1σ scatter within the bin (dotted) from the best fits derived including or omitting the PACS data (red and blue, respectively). The FIR luminosities, effective temperatures and optical properties of the low luminosity stack in L_{dust} (i.e. including/omitting PACS) are almost identical, while for the higher L_{dust} bin there is more mid-IR and PAH luminosity when the PACS data are included, and the stacked SED shows a slightly broader, slightly warmer FIR peak.

similar, suggesting that this is due to increasing dust opacity in the UV–optical with increasing redshift. This has also been noted by Dunne et al. (2011) for *H*-ATLAS galaxies, and we note that the fraction of energy emerging in the optical/FIR is also changing with redshift; again the higher redshift sources have more of their total bolometric output emerging in the FIR compared to those at lower redshifts, consistent with the aforementioned increased dust opacity at higher redshifts.

4.3.5 The range of SEDs in each stack

In addition to calculating the median stacked SED, we are also able to quantify the spread of SEDs within each bin. In Fig. 16, we demonstrate this for galaxies binned by specific star formation rate. Once more, each bin has been normalized to the mean of each SED between 0.2 and 500 μm , and the offsets between models are arbitrary for ease of comparison. As in Fig. 13, we present the transmitted galaxy templates as the solid lines, with colours corresponding to the bins of sSFR. The shaded grey regions show the region bounded by the 16th and 84th percentiles of the ensemble of normalized model SEDs at a given wavelength, $\sigma(\lambda)$ (see Appendix D for more details); this is distinct from the much smaller error on the median SED, which could be used for e.g. population studies, or comparisons with other templates (Section 5). However, this range in percentiles enables the reader to see the range of SEDs which are included in each stack, and is representative of how well any individual galaxy within a particular bin may be expected to conform to the median template. The large dispersion among the

models at optical/UV wavelengths is due to the varying degrees of dust attenuation affecting the different intrinsic stellar populations, though as the unattenuated SEDs in Fig. 14 show, the effective age of the stellar population also plays a role. In contrast, the comparable dispersion in the sub-millimetre wavelength regime ($\lambda > 80 \mu\text{m}$) is due to the varying dust properties (e.g. temperatures, relative weights of components) of the best-fitting models.

The mid-infrared wavelength range (between ~ 6 and 60 μm) shows the largest dispersion, and this is expected since we lack good observational data at this time. Constraints in this region come from the upper limits at 12, 25 and 60 μm from *IRAS* (though these are often weak constraints), the priors fed into the stochastic FIR template library (which are based on observations with *IRAS*, *ISO* and *Spitzer*) and the energy balance criterion discussed in Section 3.1. Mid-infrared data from the *WISE* satellite will dramatically improve this situation, especially at $z < 0.2$ due to the large fraction of 250 μm sources detected by *WISE* (Bond et al. 2012).

5 COMPARISON WITH EXISTING MODELS

We now compare our binned SEDs to widely used panchromatic SED templates, such as the empirical templates described in Chary & Elbaz (2001, hereafter CE01), Dale & Helou (2002, hereafter DH02) or Rieke et al. (2009, hereafter R09). Each of these models has a strong link between the dust luminosity and the shape of the SED; a link we have found to be weaker in our sample (Fig. 13).

The CE01 templates are derived as a function of their infrared luminosity, and are designed to reproduce the SEDs of existing *IRAS*-selected galaxies. The data sets used are sparsely sampled and heterogeneous, using up to 100 local galaxies at any given wavelength from 0.44 μm through the *Infrared Space Observatory* (*ISO*) and *IRAS* bands, and out to 850 μm with SCUBA, albeit with no coverage between 170 and 850 μm .

The R09 templates are based on a variety of input imaging and spectroscopy, including full optical photometry for 11 luminous and ultra-luminous infrared galaxies (LIRGs and ULIRGs) from the NASA extragalactic data base (NED), 2MASS, *IRAS*, *Spitzer* and *ISO*, as well as the GALEX models from Bruzual & Charlot (2003). The R09 models are binned in luminosity in the range $9.75 < \log_{10}(L_{\text{dust}}/L_{\odot}) < 13.0$.

The DH02 models build upon the models of Dale et al. (2001), using the sample of 69 ‘normal’ galaxies, defined according to their optical luminosities and Hubble types in Dale et al. (2000). The models have a wavelength range from 3 μm extending to radio wavelengths, derived using data from the *ISO* (between 52 and 170 μm) and SCUBA (at 450 and 850 μm) to extend the observational constraints from 3 to 850 μm . These models represent ‘global’ spectra from superpositions of local galaxy SEDs, assuming a power-law distribution for dust mass over intensity of the interstellar radiation field (ISRF), U , which is normalized such that $U = 1$ for the local ISRF (with values spanning $0.3 \leq U \leq 10^5$). The templates are constructed such that $dM_d(U) \propto U^{-\alpha} dU$, where $M_d(U)$ is the dust mass heated by an ISRF with intensity U , and the exponent (α) defines the relative contributions of the individual local galaxy SEDs to each model spectrum. DH02 specify that it is those models with $1 < \alpha < 2.5$ which describe the range of normal galaxies.

In Fig. 17, we overlay the CE01 models (colours) on the median transmitted templates from our sample (black lines with grey shaded regions to indicate the uncertainty on the median template SED following the method of Gott et al. 2001 – as opposed to the variation across 16th–84th percentiles of the stacked ensemble of

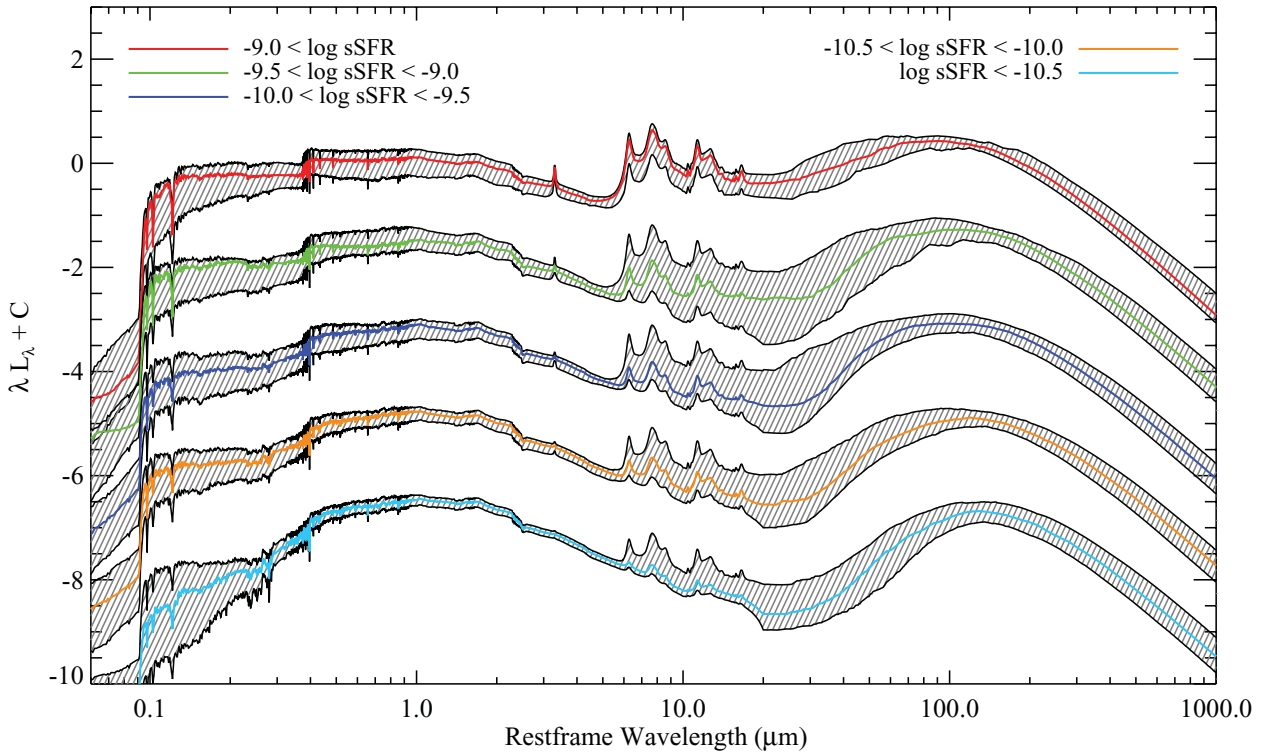


Figure 16. In addition to Fig. 13, it is possible to show the variety of different SED models within a bin of e.g. specific star formation rate. The median best-fitting transmitted SEDs are shown by the coloured solid lines corresponding to the bins of sSFR, with the 1σ spread of SEDs going into the stack shown by the shaded areas bounded by the black lines. In making these SEDs, each component SED in a particular bin of specific star formation rate has been normalized to its mean between 0.2 and 500 μm and the resulting median SEDs (plotted) have been offset from one another to prevent them from overlapping. The large variety of best-fitting models at mid-infrared wavelengths (between ~ 6 and 60 μm) is due to the lack of observational constraints in this part of the spectrum.

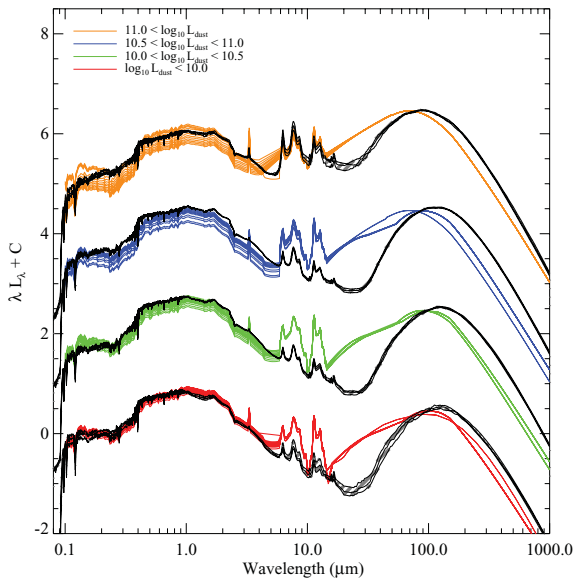


Figure 17. Comparison of our median, transmitted and luminosity-binned templates (solid black lines, with the uncertainty on the median template SED in each stack – defined using the median statistics method of Gott et al. 2001 – indicated by the shaded regions) with the templates of CE01 (shown in colour and with the luminosity bounds indicated by the legend). Each set of transmitted models with the same range in dust luminosity (indicated by the colours) has been normalized to have the same mean between 6 and 500 μm , and artificially offset in the vertical direction to prevent the models from overlapping.

galaxy SEDs as a function of wavelength in each bin as in Fig. 16), with each overlapping set of SEDs corresponding to the same range in FIR luminosities. We normalize the SEDs with corresponding values of luminosity to the mean of each SED between 6.0 and 500 μm in wavelength, and arbitrarily offset them from one another in the vertical direction for ease of comparison. Whilst there is generally good agreement between the models at optical wavelengths, the models differ considerably in the FIR, where each CE01 model peaks at shorter wavelengths (indicative of a hotter effective dust temperature) than the corresponding *H-ATLAS*-stacked SED. Whilst there is some small bias in our stacked SED in the highest two luminosity bins (see Section 4.3), this is not an issue for the bins at $\log_{10}(L_{\text{dust}}/L_{\odot}) < 10.5$ and yet the differences between the CE01 and *H-ATLAS* templates persist. The small bias in our stacking at higher luminosities (Fig. 15) is also not large enough to account for the differences in the $10.5 < \log_{10}(L_{\text{dust}}/L_{\odot}) < 11.0$ bin. We also note that the sub-mm portion of the *H-ATLAS* SEDs is well determined for all sources due to the high quality *Herschel* SPIRE data that form the foundation of this study; the differences at these wavelengths relative to the CE01 templates persist across the full luminosity range of our sample.

The largest disagreement between the two sets of models is at mid-infrared wavelengths; however, as there is a lack of observations in this region of the SED, the current mid-IR discrepancy with other templates is not significant. A full analysis with *WISE* data will be required to see if these differences persist.

In Fig. 18, we compare our templates with those of R09, this time normalized between 100 and 500 μm . The R09 templates are

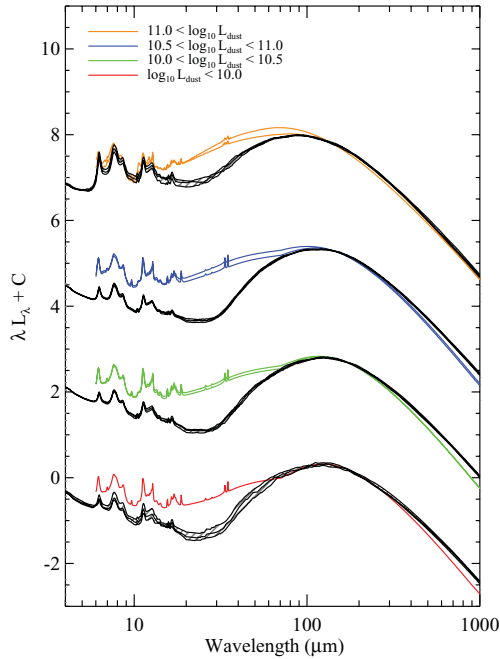


Figure 18. Comparison between the R09 and our template SEDs binned according to luminosity. As in Fig. 17, each set of SEDs is normalized between 100 and 500 μm (the Rieke et al. models are not defined in the optical) and arbitrarily offset, with our templates and uncertainties indicated by the solid line and dashed areas, respectively. Once more the luminosities of the R09 templates are shown by the colour, tabulated according to the legend. Although the R09 templates are reasonably similar to the new *H-ATLAS* templates at the lower dust luminosities, at higher dust luminosities they become increasingly warmer than the *H-ATLAS* templates.

supplied only at $\lambda > 4 \mu\text{m}$, and so the range in wavelength values is smaller than for the other two sets of models. We find that the R09 models have similar dust temperatures to our models, as demonstrated by the similar peak wavelengths of the FIR SED, but that they all have considerably brighter mid-infrared emission than our templates. Again we cannot comment further on this discrepancy until we have been able to consider the *WISE* data in the fitting.

In Fig. 19, we compare our models with the DH02 templates, which are empirically constrained at $\lambda > 3 \mu\text{m}$. Rather than limiting the comparison to the range of values of α which DH02 suggest span the range of normal galaxies in their input sample ($1.0 < \alpha < 2.5$, magenta in Fig. 19), we also compare our SEDs with the more quiescent range of DH02 templates spanning $2.5 < \alpha < 4.0$ (light blue in Fig. 19). We normalize the models at 250 μm for ease of comparison. Whilst there are DH02 models which can match our templates at the highest dust luminosities, at lower values the DH02 models suggest the presence of considerable hot dust components that are not observed in our sample of 250 μm selected galaxies, and the $\alpha > 2.5$ models are required to reproduce the far-IR temperatures that we observe. Since the DH02 models are binned by α rather than dust luminosity, we indicate the luminosity of our models being compared using the colours as indicated in the caption to Fig. 19, with the DH02 models overlaid.

These templates may be useful for studies of FIR-selected samples in the $z < 0.5$ universe. They are also useful ingredients for any evolutionary model which purports to explain the low redshift FIR/sub-mm populations detected by *Herschel*. They do not, however, appear to be representative of the high redshift ($z > 1$) population detected in *H-ATLAS* (e.g. Lapi et al. 2011). The tem-

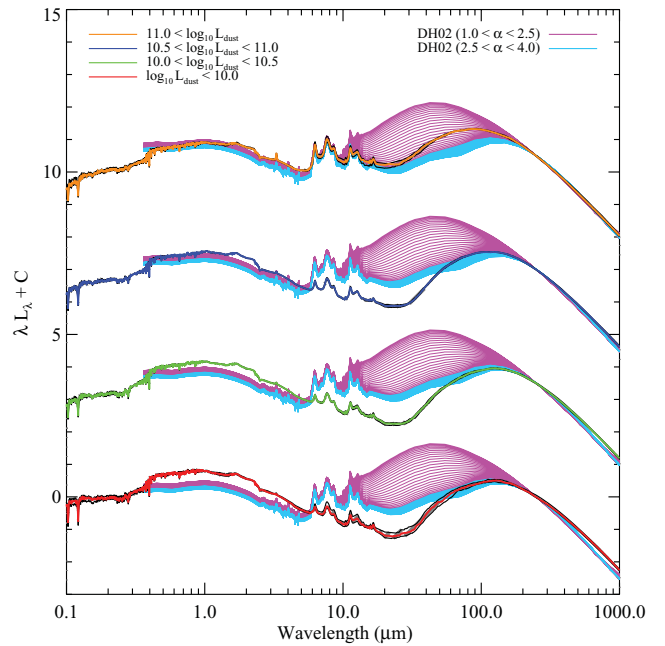


Figure 19. A comparison between our templates and those of DH02. The DH02 templates are shown in magenta for the range of α values thought by DH02 to describe normal galaxies, and in light blue for the most quiescent galaxies in the DH02 library (with $2.5 < \alpha < 4.0$). The luminosities of our templates are shown by the colour of the solid lines bounded by the shaded regions indicating the uncertainty associated with each template. For ease of comparison, each set of models being compared is normalized around 250 μm , and arbitrarily offset in the vertical direction. It is clear that the DH02 templates contain considerably hotter dust than we observe in 250 μm selected galaxies in *H-ATLAS*.

plate chosen for any SED fitting should always match the sample under investigation as selection wavelength and redshift can have an important impact on the SED types prevalent in a sample.

Irrespective of the templates to which we compare our model SEDs, the comparative lack of hot dust in our stacks is striking. Though we plan to investigate these details in future using *WISE* observations, the contribution of the mid-infrared to the total dust energy budget is not dominant; the impact of the *WISE* data near the peak of the FIR SED is likely to be small.

We intend to make these new template SEDs, binned according to their properties available to the community for further analysis, and application to other data sets via the *H-ATLAS* website⁴ and the author's website.⁵

6 CONCLUSIONS

We have determined SEDs for a total of 1402, 250 μm selected galaxies from the *Herschel-ATLAS* science demonstration catalogue with reliable counterparts and matched aperture photometry from the *u* to *K* bands from the GAMA data base. We also include far and near UV data from the *GALEX-GAMA* survey, as well as the *H-ATLAS* data from PACS and SPIRE. Of these 1402 galaxies, 1289 are well described by the model of DCE08, and we use these SEDs and the model parameter PDFs derived from the energy

⁴ <http://www.h-atlas.org>

⁵ <http://star.herts.ac.uk/~dsmith/>

balance SED fitting to determine the properties of these 250 μm selected galaxies out to $z = 0.5$.

(i) Studies of the colours of galaxies in our sample, and a suite of simulations, suggest that our sample is representative of the broader population of 250 μm galaxies out to $z < 0.35$.

(ii) The average *H*-ATLAS galaxy in our sample has a star formation rate of $\sim 4.0 M_{\odot} \text{yr}^{-1}$, $L_{\text{dust}} \approx 6.4 \times 10^{10} L_{\odot}$, and a dust to stellar mass ratio of ~ 0.4 per cent, while the median redshift is $z = 0.24$.

(iii) Our results support the idea that *IRAS*- and *H*-ATLAS-selected galaxies in the local Universe are different populations. Due to its lack of sensitivity and short selection wavelength, *IRAS* preferentially selected galaxies with larger warm dust content, and consequently these galaxies are more luminous in the infrared for a given mass of dust. The *H*-ATLAS selection at 250 μm is less biased towards strongly star-forming objects over the same redshift range because of the longer selection wavelength and far superior sensitivity compared to *IRAS*. *IRAS* misses a population of massive dusty galaxies with colder dust temperatures, as was shown previously by Vlahakis et al. (2005).

(iv) The correlation between star formation rate and dust mass presented in dC10 is also present in this sample, although *Herschel*-ATLAS-selected galaxies contain larger dust masses for a given star formation rate compared to the *IRAS*-selected sample of dC10. There is also a correlation between specific dust mass ($M_{\text{dust}}/M_{\text{stars}}$) and sSFR, which is not well reproduced by simple chemical and dust evolution models.

(v) The specific star formation rate of lower mass galaxies ($\log_{10} M_{\text{star}}/M_{\odot} < 10.2$) is higher than that of the most massive galaxies in our sample (those with $\log_{10} M_{\text{star}}/M_{\odot} > 10.6$) at all redshifts, supporting previous results that lower mass galaxies dominate the star formation rate density in the local universe.

(vi) Stacks of SEDs show that sSFR is the strongest galaxy property driving the SED shape across both the UV/optical and FIR, as first noticed in the smaller sample of DCE08. Trends with L_{dust} are much weaker since smaller mass galaxies will have low L_{dust} and yet could have the highest values of sSFR. We see a significant trend in this sample for galaxies to have more obscured optical/UV SEDs and higher reprocessed fractions with increasing redshift.

(vii) Existing templates for panchromatic SEDs of galaxies show shorter FIR peaks and excess mid-IR emission compared to median stacked SEDs of galaxies in our *H*-ATLAS sample (binned by L_{dust}) although the mid-IR discrepancy is not significant at this time due to our lack of mid-IR data to constrain this part of the SED. Templates from R09 are the closest match to ours in terms of the FIR properties although they still predict a warmer FIR peak at the highest luminosities compared to our findings. We provide a new set of panchromatic SED templates from the UV–sub-mm to enable more representative studies of dusty galaxies in the local Universe in the *Herschel* era.

(viii) Data from the *WISE* satellite, which covers the wavelength range between 3 and 23 μm , will provide valuable constraints to the mid-IR and PAH features, as well as the hot dust component of these local galaxies. It will be interesting to see if the differences between templates in the mid-IR region persists when these data are included in the fitting.

ACKNOWLEDGMENTS

The authors wish to thank the anonymous referee for his/her tireless work and insightful comments, which have substantially improved

this paper. The *Herschel*-ATLAS is a project with *Herschel*, which is an ESA space observatory with science instruments provided by European-led Principal Investigator consortia and with important participation from NASA. The *H*-ATLAS website is <http://www.h-atlas.org/>. GAMA is a joint European-Australasian project based around a spectroscopic campaign using the Anglo-Australian Telescope. The GAMA input catalogue is based on data taken from the Sloan Digital Sky Survey and the UKIRT Infrared Deep Sky Survey. Complementary imaging of the GAMA regions is being obtained by a number of independent survey programmes including *GALEX* MIS, VST KIDS, VISTA VIKING, *WISE*, GMRT and ASKAP providing UV to radio coverage. GAMA is funded by the STFC (UK), the ARC (Australia), the AAO, and the participating institutions. The GAMA website is <http://www.gama-survey.org/>. This work used data from the UKIDSS DR5 and the SDSS DR7. The UKIDSS project is defined in Lawrence et al. (2007) and uses the UKIRT Wide Field Camera (WFCAM; Casali et al. 2007). Funding for the SDSS and SDSS-II has been provided by the Alfred P. Sloan Foundation, the Participating Institutions, the National Science Foundation, the U.S. Department of Energy, the National Aeronautics and Space Administration, the Japanese Monbukagakusho, the Max Planck Society and the Higher Education Funding Council for England. The Italian group acknowledges partial financial support from ASI/INAF agreement no. I/009/10/0.

REFERENCES

- Anders P., Fritze-v. Alvensleben U., 2003, *A&A*, 401, 1063
 Baldry I. K. et al., 2010, *MNRAS*, 404, 86
 Bendo G. et al., 2010, *A&A*, 518, 65
 Bernard J.-P. et al., 2010, *A&A*, 518, 88
 Bertin E., Arnouts S., 1996, *A&AS*, 117, 393
 Blain A. W., Smail R., Ivison R. J., Kenib J.-P., Frayer D. T., 2002, *Phys. Rep.*, 369, 111
 Blain A. W., Barnard V. E., Chapman S. C., 2003, *MNRAS*, 338, 733
 Bond N. et al., 2012, *ApJ*, 750, 18
 Boselli A. et al., 2010, *A&A*, 518, 61
 Bourne N. et al., 2012, *MNRAS*, 421, 3027
 Bruzual G., 2007, *ASPC*, 374, 303
 Bruzual G., Charlot S., 2003, *MNRAS*, 344, 1000
 Bundy K. et al., 2006, *ApJ*, 651, 120
 Bundy K., Fukugita M., Ellis R. S., Targett T. A., Belli S., Kodama T., 2009, *ApJ*, 697, 1369
 Calura F., Pipino A., Metteucci F., 2008, *A&A*, 479, 669
 Carter D. et al., 2009, *MNRAS*, 397, 695
 Casali M. et al., 2007, *A&A*, 467, 777
 Chabrier G., 2003, *PASP*, 115, 763
 Chapman S. C., Blain A. W., Smail I., Ivison R. J., 2005, *ApJ*, 622, 772
 Charlot S., Fall S. M., 2000, *ApJ*, 539, 718
 Chary R., Elbaz D., 2001, *ApJ*, 556, 562 (CE01)
 Ciliegi P. et al., 2005, *A&A*, 441, 879
 Clements D. L., Dunne L., Eales S., 2010, *MNRAS*, 403, 274
 Collins C. A. et al., 2009, *Nat*, 458, 603
 Collister A. A., Lahav O., 2004, *PASP*, 116, 345
 Contursi A., Boselli A., Gavazzi G., Bertagna E., Tuffs R., Lequeux J., 2001, *A&A*, 365, 11
 Coppin K. E. K. et al., 2006, *MNRAS*, 273, 1621
 Cortese L. et al., 2012, *A&A*, 540, 52
 Cowie L. L., Songaila A., Hu E. M., Cohen J. G., 1996, *AJ*, 112, 839
 da Cunha E., Charlot S., Elbaz D., 2008, *MNRAS*, 388, 1595 (DCE08)
 da Cunha E., Eminian C., Charlot S., Blaizot J., 2010, *MNRAS*, 403, 1894 (dC10)
 Dale D. A., Helou G., 2002, *ApJ*, 576, 159 (DH02)
 Dale D. A. et al., 2000, *AJ*, 120, 583

- Dale D. A., Helou G., Contursi A., Silbermann N. A., Kolhatkar S., 2001, *ApJ*, 549, 215
- Dale D. A. et al., 2012, *ApJ*, 745, 95
- Devlin M. J. et al., 2009, *Nat*, 458, 737
- Draine B. T. et al., 2007, *ApJ*, 663, 866
- Driver S. P. et al., 2011, *MNRAS*, 413, 971
- Driver S. P. et al., 2012, preprint (arXiv:1209.0259)
- Dunne L., Eales S., 2001, *MNRAS*, 327, 697
- Dunne L., Eales S., Edmunds M., Ivison R., Alexander P., Clements D. L., 2000, *MNRAS*, 315, 115
- Dunne L. et al., 2011, *MNRAS*, 417, 1510
- Dwek E., 1998, *ApJ*, 501, 643
- Dye S. et al., 2009, *ApJ*, 703, 285
- Dye S. et al., 2010, *A&A*, 518, 10
- Eales S., Lilly S., Gear W., Dunne L., Bond J. R., Hammer F., Le Fèvre O., Crampton D., 1999, *ApJ*, 515, 518
- Eales S. et al., 2009, *ApJ*, 707, 1779
- Eales S. et al., 2010, *PASP*, 122, 499
- Fioc M., Rocca-Volmerange B., 1997, *A&A*, 326, 950
- Fixsen D. J., Dwek E., Mather J. C., Bennett C. L., Shafer R. A., 1998, *ApJ*, 508, 123
- Galamez M., Madden S. C., Galliano F., Hony S., Bendo G. J., Sauvage M., 2011, *A&A*, 532, 56
- Gott J. R., III, Vogeley M. S., Podarin S., Ratra B., 2001, *ApJ*, 549, 1
- Griffin M. et al., 2010, *A&A*, 518, L3
- Hill D. T. et al., 2011, *MNRAS*, 412, 765
- Hopkins P. F., Bundy K., Hernquist L., Ellis R., 2007, *ApJ*, 659, 976
- Hughes et al., 1998, *Nat*, 394, 241
- Hwang H. S. et al., 2010, *MNRAS*, 409, 75
- Ibar E. et al., 2010, *MNRAS*, 409, 38
- Jimenez R., Jorgensen U. G., Thejll P., Macdonald J., 1995, *MNRAS*, 275, 1245
- Jimenez R., Macdonald J., Dunlop J., Padoan P., Peacock J. A., 2004, *MNRAS*, 349, 240
- Kennicutt R. C., Jr, et al., 2003, *PASP*, 115, 928
- Kóvács A., Chapman S. C., Dowell C. D., Blain A. W., Ivison R. J., Smail I., Phillips T. G., 2006, *ApJ*, 650, 592
- Kramer C. et al., 2010, *A&A*, 518, 67
- Lapi A. et al., 2011, *ApJ*, 742, 24
- Lawrence A. et al., 2007, *MNRAS*, 379, 1599
- Lehmer B. D. et al., 2005, *ApJS*, 161, 21
- Lonsdale C. et al., 2003, *PASP*, 115, 897
- Magnelli B. et al., 2012, *A&A*, 539, 155
- Maraston C., 2005, *MNRAS*, 362, 799
- Morgan H. L., Edmunds M. G., 2003, *MNRAS*, 343, 427
- Morrissey P. et al., 2007, *ApJS*, 173, 682
- Moshir M., Kopman G., Conrow T. A. O., 1992, Explanatory Supplement to the IRAS Faint Source Survey, Version 2., JPL D-10015 8/92 (Pasadena JPL)
- Negrello M. et al., 2010, *Sci*, 330, 800
- Pacifici C., Charlot S., Blaizot J., Brinchman J., 2012, *MNRAS*, 421, 2002
- Pascale E. et al., 2011, *MNRAS*, 415, 911
- Pfarr J., Maraston C., Tonini C., 2012, *MNRAS*, 422, 3285
- Pierini D., Gordon K. D., Witt A. N., Madsen G. J., 2004, *ApJ*, 617, 1022
- Pietrinferni A., Cassisi S., Salaris M., Castelli F., 2004, *ApJ*, 612, 168
- Pilbratt G. L. et al., 2010, *A&A*, 518, L1
- Planck Collaboration, 2011, *A&A*, 536, 16
- Poglitsch A. et al., 2010, *A&A*, 518, L2
- Pope A. et al., 2006, *MNRAS*, 370, 1185
- Popescu C. C., Tuffs R. J., Volk H. J., Pierini D., Madore B. F., 2002, *ApJ*, 567, 221
- Pozzetti L. et al., 2010, *A&A*, 523, 13
- Puget J.-L., Abergel A., Bernard J.-P., Boulanger F., Burton W. B., Désert F.-X., Hartmann D., 1996, *A&A*, 308, 5
- Rieke G. H., Alonso-Herrero A., Weiner B. J., Pérez-González P. G., Blaylock M., Donley J. L., Marcellac D., 2009, *ApJ*, 692, 556 (R09)
- Rigby E. E. et al., 2011, *MNRAS*, 415, 2336
- Rowan-Robinson M. et al., 2010, *MNRAS*, 409, 2
- Silva L., Granato G. L., Bressan A., Danese L., 1998, *ApJ*, 509, 103
- Skibba R. et al., 2011, *ApJ*, 738, 89
- Skrutskie M. et al., 2006, *AJ*, 131, 1163
- Smail I., Ivison R. J., Blain A. W., 1997, *ApJ*, 490, 5
- Smith D. J. B., Jarvis M. J., 2007, *MNRAS*, 378, 49
- Smith D. J. B., Simpson C., Swinbank A. M., Rawlings S., Jarvis M. J., 2010, *MNRAS*, 404, 1089
- Smith D. J. B. et al., 2011, *MNRAS*, 416, 857
- Somerville R. S., Gilmore R. C., Primack J. R., Dominguez A., 2012, *MNRAS*, 423, 1992
- Sutherland W., Saunders W., 1992, *MNRAS*, 259, 413
- Swinbank A. M. et al., 2009, *MNRAS*, 400, 1121
- Tuffs R. J., Popescu C. C., Völk H. J., Kyllafis N. D., Dopite M. A., 2004, *A&A*, 419, 821
- Vazquez G. A., Leitherer C., 2005, *ApJ*, 621, 695
- Vlahakis C., Dunne L., Eales S., 2005, *MNRAS*, 364, 1253
- Wang L., Rowan-Robinson M., 2009, *MNRAS*, 398, 109
- Weiß A. et al., 2009, *ApJ*, 707, 1201
- Willmer C. N. A., Rieke G. H., Le Floch E., Hinz J. L., Engelbracht C. W., Marcellac D., Gordon K. D., 2009, *ApJ*, 138, 146
- Wright E. L. et al., 2010, *AJ*, 140, 1868
- York D. G. et al., 2000, *AJ*, 120, 1579

APPENDIX A: STACKING PDFs AND CHOICE OF COLD TEMPERATURE PRIOR

A1 Derivation and interpretation of stacked PDFs

In this paper, we make considerable use of stacked PDFs, which are our best estimates of the distribution of the values of a given parameter amongst the sources in a sample, convolved with our ability to constrain them. To see why this latter point might be important, imagine we have individual PDFs for a certain parameter which has very weak constraints, all the PDFs will therefore appear flat. The distribution of the medians of these PDFs (i.e. the median-likelihood estimates for that particular parameter) will be centred near the middle of the range (since the PDFs are all individually flat) and will have a narrow scatter (since all medians are almost the same). If we only considered the median-likelihood values, we might naively assume that we know the parameter distribution for the population quite accurately, and that there was little scatter within the population, even though in truth we merely had little ability to constrain that parameter. This is an extreme example and does not apply to the parameters we are exploring in this paper, but it illustrates why we wish to present the stacked marginalized PDFs and not simply the distributions of the median likelihood values.

To derive values of stacked PDFs, we start with the values in each bin of the ensemble of PDFs that we wish to stack. For the value of the stacked PDF in each bin we use the mean of the ensemble of values in that bin. To estimate the error associated with the derived stacked PDF in each bin, we simply use a symmetric value corresponding to the mean of the 16–84th percentiles of the cumulative frequency distribution of the values for each galaxy in that bin.

A2 Choice of the T_{cold} prior distribution

When choosing a prior distribution for a particular parameter in the stochastic libraries of SEDs, we must ensure that our choice of prior does not bias our results. This was of particular concern for the prior on T_{cold} since the stacked PDFs do not always show a peak in the range of the prior, but for some samples, increase towards the lowest bounds of the prior. We wanted to determine whether or not this was an indication that we should use a broader prior on T_{cold} .

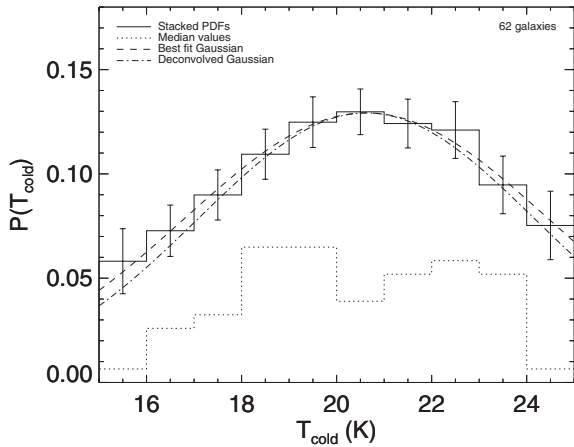


Figure A1. The stacked PDFs (solid line, with error bars) for those 59 galaxies with PACS 160 μm detections with $S_{250} > 120$ mJy at $z < 0.20$. We overplot the median values of the individual PDFs for these galaxies (dotted histogram), along with the best-fitting Gaussian approximation of the PDF. The deconvolved version (described in the text) is shown by the dot-dashed line and has a standard deviation of 3.54 ± 0.41 K.

To address this issue, we considered the properties of the galaxies in our PACS-complete sample (see Section 4.1.2), which, as we showed in Section 4.1.2 and Fig. 6, are representative of the full range of colours in *H*-ATLAS sources and, by virtue of their being detected in our PACS data, have our best constraints on T_{cold} .

We stacked the PDFs for these galaxies, and the results are shown in Fig. A1, in which the best-fitting Gaussian approximation to the stacked PDF is shown as the dashed line, and a histogram of the median values of each individual PDF that went into the stack by dotted lines. The best-fitting Gaussian model of the stacked PDF has a standard deviation of 3.84 ± 0.41 K. In order to assess the true range of T_{cold} that is present in our sample, we determined the deconvolved best-fitting Gaussian, by subtracting the mean of the individual 1σ errors on T_{cold} for each galaxy ($1.47\text{ K} \pm 0.19$) in quadrature, leaving a 1σ uncertainty on the range of T_{cold} in our sample as 3.54 ± 0.41 K. The best-fitting deconvolved Gaussian is shown as the dot-dashed line in Fig. A1. We find that 85 percent of the true T_{cold} PDF lies within the bounds of our temperature prior, with only ~ 6 per cent of the PDF colder than 15 K, and approximately 9 per cent warmer than 25 K.

In that case, why not make a T_{cold} prior which is wider and therefore encompasses the full range of temperatures possible in the cold ISM? The reason behind not doing so is the strong non-linear dependence of the M_{dust} parameter on T_{cold} when the value of T_{cold} is below ~ 15 K. At such cold temperatures, the SPIRE bands no longer sample the Rayleigh-Jeans part of the SED (where M_{dust} scales relatively linearly with T_{cold}) but are nearer the peak where the dependence on temperature is steeper.

The fitting becomes more prone to errors on the determination of T_{cold} at low values, since the energy balance is not much affected by the addition of very cold dust to the SED (which contributes little to the total L_{dust}). Dust colder than 15 K is essentially invisible to our model (or any other for that matter), which combined with the added sensitivity of mass to temperature at low T_{cold} results in an asymmetry in the error on the dust mass; we have a larger overestimation of the mass when T_{cold} is underestimated (statistically likely to happen 50 per cent of the time) compared to the size of our underestimate in M_{dust} when T_{cold} is overestimated.

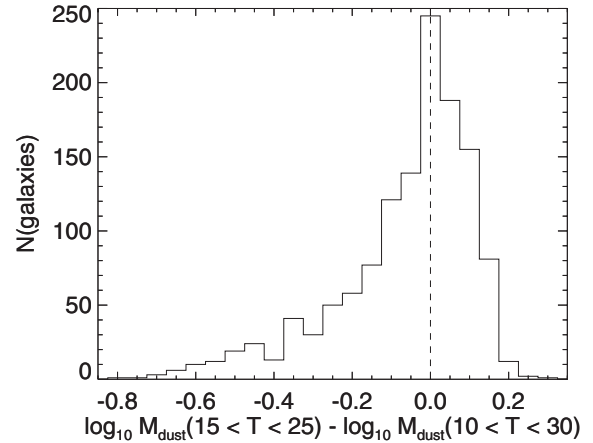


Figure A2. The difference in the dust mass estimates that we determine for the galaxies in our sample depending on whether we use the broader ($10 < T_{\text{cold}} < 30$) or narrower ($15 < T_{\text{cold}} < 25$) prior. The asymmetry in this histogram is caused by a greater sensitivity to temperature at cold temperatures.

To demonstrate this, we created a hypothetical library of 1000 model galaxies with Gaussian temperature and mass distributions, and simply re-estimated the dust mass after adding on simulated measurement errors to the true temperature distribution, using the relationship between temperature and dust mass for a modified greybody emission profile shown in equation 3 of Dunne et al. (2011). In these simple simulations, measurement errors introduced a systematic anti-correlation between the estimated temperature and estimated dust mass. In Fig. A2, we show a histogram of the difference in our median estimated dust masses, derived using the broader and narrower T_{cold} prior distributions. The effect is stronger at the coldest temperatures, which occur more often with the broader T_{cold} prior, with some dust masses being overestimated by in excess of 0.5 dex. In order to limit the effects of this unphysical bias towards large dust mass estimates in the colder galaxies in our sample, we decided to use the narrower prior on T_{cold} .

We confirm the effects on T_{cold} by re-running the fitting using a wider T_{cold} prior (10–30 K) on sub-samples of galaxies which represent typical selections within the main analysis and compare these results to those using the T_{cold} prior from DCE08 (15–25 K).

We split our sample into five sub-sets, limited to $z < 0.2$, to limit the possible influence of cosmic evolution on our results:

- (i) galaxies in our PACS-complete sub-sample,
- (ii) galaxies detected at $> 5\sigma$ in both PACS bands and $> 3\sigma$ at 350 and 500 μm ,
- (iii) galaxies with at least one PACS $\geq 5\sigma$ detection,
- (iv) galaxies detected at $\geq 3\sigma$ at 350 μm ,
- (v) all galaxies in our sample.

Of course, all galaxies discussed here are detected at $\geq 5\sigma$ at 250 μm , since this is how our sample is defined.

In Table A1, we show the median-likelihood values of T_{cold} derived from the PDFs for each sub-sample. None of the stacked PDF median-likelihood T_{cold} values varies by more than ~ 0.6 K when the broader prior is used rather than the narrower prior; the impact on our global estimates of T_{cold} is therefore minimal. When we use the broad prior on T_{cold} , we find that 13 per cent of our sample have T_{cold} values of < 15 K, approximately in line with the 6 per cent that we expect from studying the PACS-complete sample.

Table A1. The effects of our choice of prior distribution on our median-likelihood estimates of T_{cold} . The left-hand column indicates the selection of each different sub-sample, in addition to the requirement that all sources have 5σ detections in the SPIRE 250 μm band. The middle two columns indicate the T_{cold} estimates determined for each sub-sample with the two prior distributions, while the right-hand column shows the difference. Each sub-sample has been limited to $z < 0.2$, in order to limit the impact of evolution with redshift on these values.

Detections	$10 < T_{\text{cold}} < 30$	$15 < T_{\text{cold}} < 25$	$\Delta(T_{\text{cold}}, \text{prior})$
PACS complete sub-sample	20.66	20.61	0.05
All PACS 5σ , S350 and S500 $>3\sigma$	21.59	21.49	0.10
P100 or P160 $>5\sigma$	21.39	21.13	0.26
S350 $>3\sigma$	18.61	19.19	-0.58
S250 $>5\sigma$ only	19.06	19.41	-0.35

When we consider the median temperature estimates with each prior in Table A1, we see that the second two samples – which require 5σ PACS detections – have higher median values due to the removal of the coldest sources from the sub-sample; these sources are generally undetected in our comparatively shallow PACS data. The last two sub-samples in Table A1 have lower values of T_{cold} , and are mostly undetected by PACS; in particular, the 350 μm selection criterion preferentially picks the colder sources in the catalogue, with SEDs peaking at longer wavelengths.

In summary, we have used the DCE08 $15 < T_{\text{cold}} < 25$ K temperature priors for the following reasons.

(i) Simulations and studies of the PACS-complete sample suggest that we can explain our data adequately using the DCE08 prior.

(ii) The narrower prior also limits the impact of T_{cold} errors on M_{dust} .

(iii) Detailed studies using a variety of multi-wavelength data and modelling techniques see no evidence for substantial cold dust components with temperatures lower than 15 K in the kind of dust-rich spiral galaxies being investigated here (e.g. Dunne & Eales 2001; Popescu et al. 2002; Vlahakis et al. 2005; Draine et al. 2007; Willmer et al. 2009; Bendo et al. 2010; Bernard et al. 2010; Boselli et al. 2010; Kramer et al. 2010).

APPENDIX B: DEFINING THE GOOD FITS

We took a selection of best-fitting model SEDs, and varied their photometry according to a set of Gaussian distributions with a median of zero and a standard deviation equal to the minimum photometric error in each band (i.e. the values added in quadrature, as defined in Section 2). These values were chosen since they were the dominant source of error for bright sources. We then removed a sub-set of photometry to reflect the heterogeneity within our real data set, and re-calculated their properties 1000 times each. The resulting histograms of χ^2 values (e.g. Fig. B1) enabled us to estimate the number of degrees of freedom given that particular sub-set of photometry, by performing a simple minimization of equation (B1) to the derived χ^2 PDFs:

$$P \propto \frac{1}{2^{(N_{\text{dof}}/2)} \Gamma(N_{\text{dof}}/2)} (\chi^2)^{(N_{\text{dof}}/2)-1} e^{-\chi^2/2}, \quad (\text{B1})$$

where $\Gamma(x)$ represents the Gamma function, N_{dof} the number of degrees of freedom and χ^2 the median χ^2 value for each bin. Due to the relatively small redshift range covered by our sample, we average each solution and determine that the relationship between the number of degrees of freedom (N_{dof}) and the number of photometric

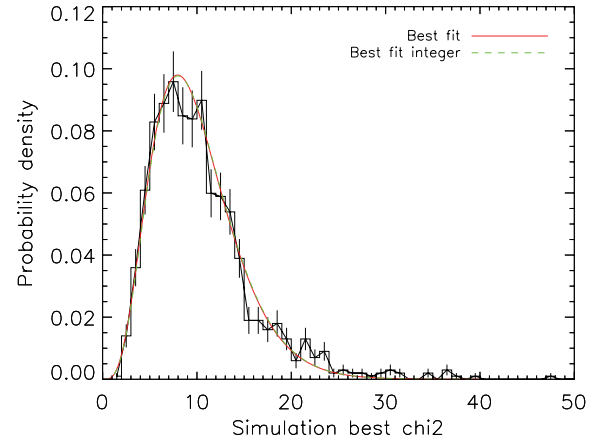


Figure B1. The distribution of χ^2 values for the 1000 galaxy simulations referred to in the text. The shape of the resulting histogram is well described by equation (B1), and depends on only one parameter, the number of degrees of freedom for that particular combination of input photometry (N_{dof}). In this way, N_{dof} can then be determined for each combination of photometry by simply minimizing equation (B1). By fitting a quadratic to these results, we may relate N_{dof} and N_{bands} . The resulting relationship is shown in equation (B2). The combination of equations (B1) and (B2) allows us to define 99 per cent confidence intervals and in turn determine which galaxies in our sample are well described by our model.

bands with measurements (N_{bands}) is given by equation (B2):

$$N_{\text{dof}} \approx (-2.820 \pm 0.745) + (0.661 \pm 0.132)N_{\text{bands}} + (7.91 \pm 5.50 \times 10^{-3})N_{\text{bands}}^2. \quad (\text{B2})$$

With this information, we are then able to use equation (B1), in conjunction with the number of degrees of freedom estimate from equation (B2), to determine a 99 per cent confidence interval on χ^2 . Those galaxies outside the interval on χ^2 have less than 1 per cent chance of being consistent with our model. In this way, we may remove those ‘bad fits’ from further analysis. We derived equation (B2) using galaxies with between 6 and 19 detections, so these values constitute the bounds on N_{bands} over which we believe it is valid.

Finally, in comparing our simulations to our real sample, we note that in contrast to our simulations, the photometric errors used in our SED fitting are not strictly Gaussian due to problems associated with e.g. deblending or calibration issues, particularly in regions neighbouring saturated stars; however, the difference is not expected to be large.

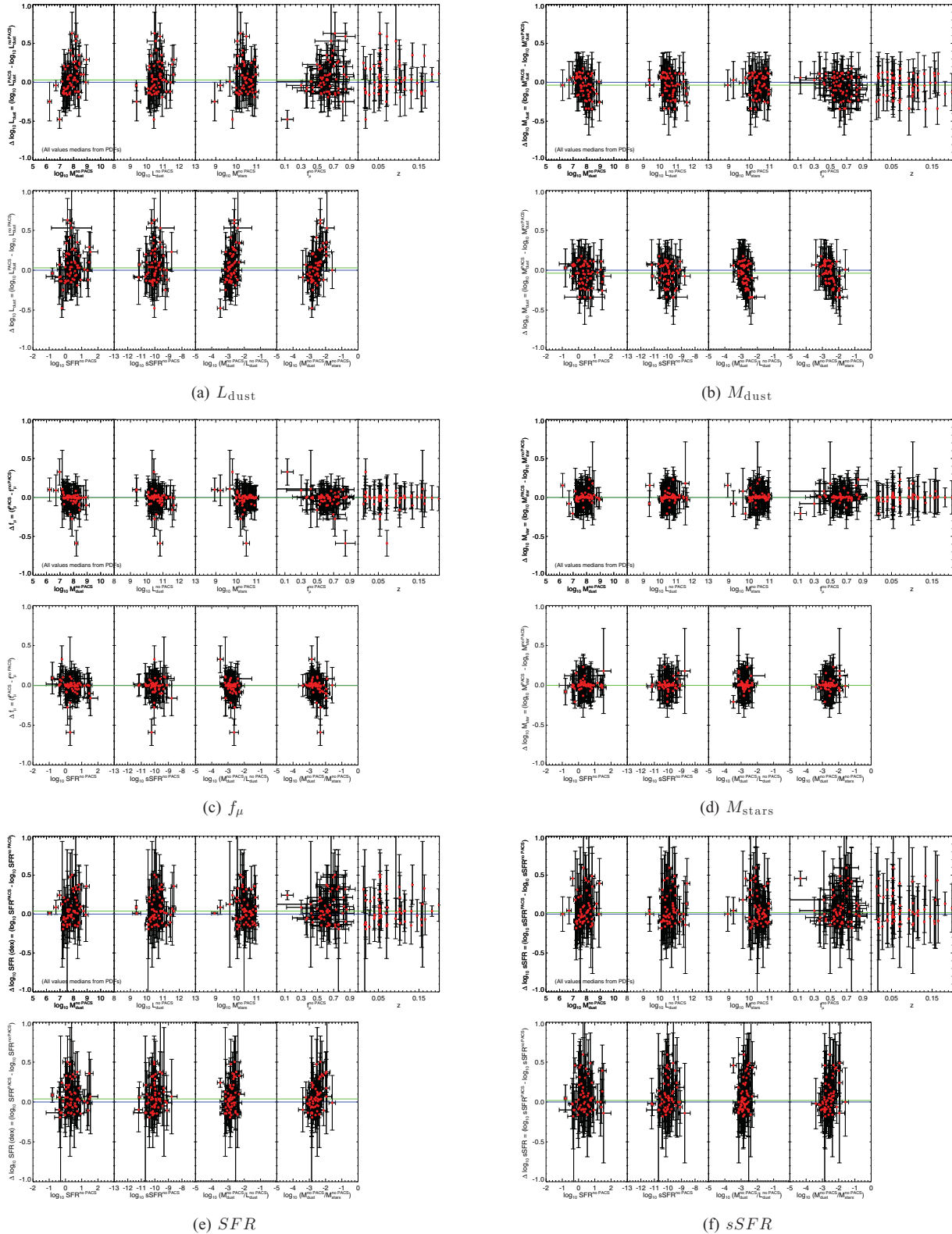


Figure C1. Variation in (a) L_{dust} , (b) M_{dust} , (c) f_{μ} , (d) M_{stars} , (e) SFR and (f) sSFR as a function of each of the parameters discussed in this paper for the PACS-complete sample described in Section 4.1.2. The data points are shown as red circles, with horizontal error bars indicating the uncertainties derived neglecting the PACS data, and the vertical position derived according to equation (C1), considering the asymmetric errors on the median likelihood values for each parameter. The blue horizontal line indicates $\Delta Q = 0$ whilst the green horizontal line denotes the difference between the median values of the stacked PDFs for the whole PACS complete sample when the PACS data are included and when they are omitted.

APPENDIX C: ADDITIONAL TESTS FOR BIAS IN THE FITTING

Due to the complexity of the energy-balance SED fitting method, we wanted to perform additional checks for bias in the derived parameters, and determine which parameters depend on one another.

In turn, we calculate the variation on our key parameters (L_{dust} , M_{dust} , f_{μ} , M_{stars} , SFR and sSFR) introduced in our ‘PACS-complete’ sample when the PACS data are included and when they are omitted from the fitting, as a function of each of the derived parameters included in this analysis. We consider the difference in each parameter Q (e.g. L_{dust} , sSFR, etc.):

$$\Delta Q = Q^{\text{PACS}} - Q^{\text{noPACS}}, \quad (\text{C1})$$

where Q^{PACS} and Q^{noPACS} are the median likelihood estimates for a particular source including or ignoring the PACS information in the fitting. In this way, we are able to probe for a skew in the bias between estimates of a parameter, e.g. do we overestimate L_{dust} for particular L_{dust} when galaxies are not detected by PACS? Even though we have used our stacked PDFs to probe for overall bias and found that it is minimal for all of the key parameters that we discuss in this paper (they are detailed in Table 2), it is still possible that ΔQ is skewed for some parameter combinations. In Fig. C1, we plot these values along with their error bars. The individual data points are shown as red circles, with error bars in the horizontal direction derived in the absence of the PACS data. The blue solid line indicates zero offset, while the green solid line the median of the stacked PDF for all galaxies in the ‘PACS-complete’ sample that we explore here.

In Fig. C1(a), we consider possible bias in L_{dust} . We find that there is a skewed bias between ΔL_{dust} and $M_{\text{dust}}^{\text{noPACS}}$; though the scatter is large, these tests suggest that L_{dust} is underestimated at high M_{dust} and underestimated at lower values in the absence of PACS data, though the offset averaged across the whole range of $M_{\text{dust}}^{\text{noPACS}}$ is small. ΔL_{dust} appears broadly unbiased across all values of $L_{\text{dust}}^{\text{noPACS}}$, while there is little evidence for any bias with respect to M_{stars} , f_{μ} , (specific) SFR or redshift. There is evidence for bias in L_{dust} with respect to $M_{\text{dust}}/L_{\text{dust}}$ and $M_{\text{dust}}/M_{\text{star}}$, though these biases are dominated by the bias in M_{dust} already discussed.

Fig. C1(b) shows the variation in ΔM_{dust} as a function of the same key parameters, suggesting that there may be a tendency to overestimate M_{dust} in the absence of PACS data at the highest dust masses probed by this study and there is a small tendency for dust masses to be overestimated in the absence of PACS data on average (comparing the blue and green horizontal lines in Fig. C1). The related parameters $M_{\text{dust}}^{\text{noPACS}}/L_{\text{dust}}^{\text{noPACS}}$ and $M_{\text{dust}}^{\text{noPACS}}/M_{\text{stars}}^{\text{noPACS}}$ also show evidence for skew.

Figs C1(c) and (d) show the variation in Δf_{μ} and ΔM_{stars} ; it is clear that they are unbiased with respect to the other model outputs that we use in this paper, as probed by the ‘PACS-complete’ sample. Though the spread in ΔSFR and ΔsSFR is larger, reflected in the larger error bars in Fig. C1(e) and (f), it is difficult to discern any skew or bias between these parameters and the other model outputs.

APPENDIX D: STACKING SAMPLES OF SEDS

In order to calculate the median of an ensemble of SEDs, we first normalize each individual SED to the mean between 0.2 and 500 μm

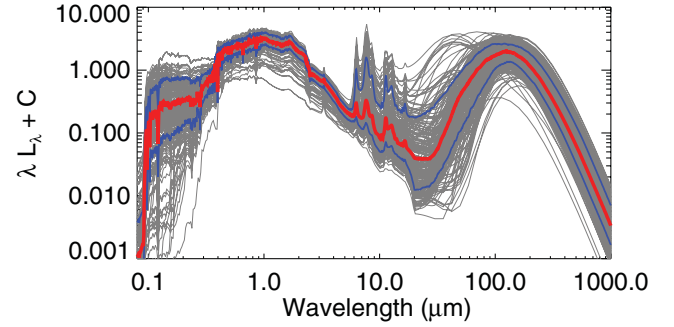


Figure D1. Individual best-fitting SEDs (grey points) are first normalized between 0.2 and 500 μm , and then the median (the red line) and 16th and 84th percentiles of the ensemble (blue lines) are calculated as a function of wavelength. This particular example shows the stacked SEDs of those 216 galaxies with good best-fitting models at $z < 0.35$ and with $10.0 < \log_{10}(L_{\text{dust}}/L_{\text{solar}}) < 10.5$.

(in units of λF_{λ}), such that each template is given equal weighting in the stack, and then take the median of the ensemble of normalized SED values in each wavelength bin. We also determine the 16th and 84th percentiles of the cumulative SED distribution as a function of wavelength. These values provide a measure of the spread in the SEDs of the galaxies which go into the stack, in contrast to the estimated error on the median template shown in Fig. 16, which is determined using the median statistics method of Gott et al. (2001). Our method of determining the range of values in our SED stacks (i.e. the 16–84th percentiles) is illustrated in Fig. D1, in which the individual best-fitting SEDs that go into the median template (in this case for 216 galaxies with good fits, at $z < 0.35$, and with $10.0 < \log_{10}(L_{\text{dust}}/L_{\text{solar}}) < 10.5$) are shown in grey, while the median and the aforementioned percentiles are overlaid in red and blue lines, respectively.

Note that for the purposes of calculating these stacked templates, we bin according to the best-fitting values returned from the fitting code rather than the medians of the PDF that we use for analysis elsewhere. This distinction is noteworthy since we determine only the best-fitting model SEDs for each galaxy (as opposed to the full PDF at each wavelength). Whilst there is generally excellent agreement between the best-fitting and the median-likelihood estimates of any given parameter, the two may differ in individual cases, adding unrealistic outliers in the stacked SEDs if median-likelihood values are used for these purposes.

Whilst this method of stacking SEDs determines templates designed to be representative of a typical galaxy in a given sample (or sub-sample) of galaxies, it is important to note that we do not expect such templates to reproduce the total cosmic SED (e.g. Hill et al. 2011; Somerville et al. 2012; Driver et al. 2012), which would require calculating the sum of the emergent SEDs without prior normalization. We leave further discussion of this topic for a future publication.

This paper has been typeset from a $\text{\TeX}/\text{\LaTeX}$ file prepared by the author.